Available online at www.sciencedirect.com
ScienceDirect
Journal of Magnesium and Alloys xxx (xxxx) xxx
www.elsevier.com/locate/jma

Full Length Article

Mechanistic investigation of highly bendable magnesium alloy sheet fabricated by short-process manufacturing

Shiwei Xu[a,b,c], Peijie Xiao[a,b,c], Xiaofan Wu[a], John Holmes[d], Frédéric Mompiou[e], Zhenyu Xiao[a,b], Chen Jin[f], Tianjiao Li[g], Kuaishe Wang[h], Zhuoran Zeng[b,c,d,i,*]

[a] College of Mechanical and Vehicle Engineering, Hunan University, Changsha 410082, China
[b] State Key Laboratory of Advanced Design and Manufacturing Technology for Vehicle, Hunan University, Changsha 410082, China
[c] Suzhou Research Institute of Hunan University, Suzhou 215131, China
[d] College of Engineering, Computing and Cybernetic, Australian National University, ACT 2601, Australia
[e] CEMES-CNRS, Université de Toulouse, 29 rue J. Marvig, Toulouse 31055, France
[f] Qinghai Salt Lake Teli Magnesium Co., Ltd., Xining 810000, China
[g] International Joint Laboratory for Light Alloys (Ministry of Education), College of Materials Science and Engineering, Chongqing University, Chongqing 400044, China
[h] School of Metallurgical Engineering, Xi'an University of Architecture & Technology, Xi'an 710055, China
[i] College of Materials Science and Engineering, Hunan University, Changsha 410082, China

Received 10 July 2023; received in revised form 26 August 2023; accepted 15 September 2023
Available online xxx

Abstract

In this study, a commercial magnesium alloy AZ31 (Mg-3Al-1Zn-0.3Mn) sheet through a short manufacturing process was found to be ductile and highly formable in bending. Despite possessing a strong basal texture, the short-processed sheet without any annealing can be bent at a small radius, only 0.2 times its thickness in the 90° bending test. Additionally, it could withstand direct deformation by repeated folding-flattening. The *in-situ* microstructural characterization reveals that extension twin bands with strain localization appear in the bending area. During subsequent flattening, these twin bands underwent detwinning, reducing local strain concentrations and enabling further bending deformation. Such outstanding bend formability originated from the significant ⟨a⟩-type dislocation loops slipping on the prismatic crystal planes within dynamic-recrystallized grains. These grains underwent a uniform refinement to several microns in the short manufacturing process and exhibited low residual strain. The active prismatic dislocation slip within refined grains was due to its much lower relative activation stress to basal slip ($CRSS_{prism}$/ $CRSS_{basal}$ of only ∼1.6) owing to the effective grain boundary hardening. Furthermore, the prismatic dislocation activity was further enhanced when bypassing Al-Mn nano-particles during motion, leaving debris and loops that facilitated easy multiplication.

Keywords: Magnesium; Deformation; Texture; *In-situ* characterization; Dislocation slip.

1. Introduction

Magnesium (Mg) is the lightest structural metal and its alloys have a great potential to be widely used in automotive, railway, aerospace, and consumer electronics industries for lightweighting and energy saving [1]. For example, the usage of Mg alloys in North American-built family vehicles has been expanding by 10–14% annually in recent years [2]. The rationale is evident—a 10% weight reduction from a total vehicle weight can improve fuel economy by 4–8%. In sectors like automotive manufacturing, there exists a pressing demand for high-performance and cost-effective thin sheets of Mg alloys to craft structural components, including body pan-

* Corresponding author at: State Key Laboratory of Advanced Design and Manufacturing Technology for Vehicle, Hunan University, Changsha 410082, China.
E-mail address: zhuoran.zeng@anu.edu.au (Z. Zeng).

https://doi.org/10.1016/j.jma.2023.09.026

els and floor pans, as substitutes for the current employment of aluminum and steel sheets.

However, the manufacturing of Mg alloy sheets normally requires complex thermomechanical processes including multiple passes of rolling with several intermediate reheats. Due to the small process window, the thickness reduction in the breakdown mill is usually controlled to be around 10% in each pass [3], and restricted to 10–30% per pass after breakdown to avoid edge cracking [4]. The protracted manufacturing cycle results in elevated expenses and diminished efficiency in sheet manufacturing. Moreover, the utilization of Mg alloy sheets faces an additional constraint posed by their inadequate bend formability at ambient temperatures. In many industries especially automotive, transportation, and consumer electronics, bend formability is a key performance requirement of a sheet metal, which has to be bent into desired shapes (normally V-shape, U-shape, and channel) [5,6]. In vehicle manufacturing, for instance, high bend formability stands as a prerequisite property for processes like the hemming, which is used to join two sheet metal panels by bending the flange of the outer panel over the inner one. The deficiency in bend formability of Mg sheets can be demonstrated by its larger minimum bend radius, about 5T – 13T (times of sheet thickness) [7], than that of 3000 and 5000-series Al alloy (0T – 4T) [8]. The low bend formability of the sheet is predominantly due to an insufficient number of deformation modes imposed by its hexagonal structure and the strong basal texture developed during the sheet rolling process [9,10].

Despite the substantial industrial demand for enhancing the bend formability of Mg alloy sheets, the research about bendability is still limited [11–16], compared with considerable studies for enhancing the ductility and stretch formability of Mg alloys [17–26]. So far, the bend formability of Mg alloy sheets was predominantly enhanced by texture weakening that allows the increased activity of basal dislocation slip. The 'E-form' of Mg-3Al-1Zn-0.3Mn (AZ31) sheet has weakened basal texture and a small minimum bend radius of ∼5T [27] due to the Ca addition to AZ31 alloy [20]. Without Ca addition, the minimum bend radius of the AZ31 rolling sheet was reportedly as small as ∼3T, but it has to be rolled with ultra-high speed (2000 m/min) [28], which is at least ten times more than the speed of Al alloy rolling [29]. Subject to such a high rolling speed, the center of the AZ31 sheet has a weakened non-basal texture that is significantly split towards the rolling direction (RD). The origin of texture weakening in the high-speed-rolled AZ31 is not clear, but such an extreme processing condition makes it very challenging to be widely applied [29]. For the conventional AZ31 alloy rolling sheet (0.5–6.3 mm in thickness) with typical basal texture, the minimum bend radius is 5.5T in the fully annealed state (AZ31B-O) and 8T after work hardened by rolling and then partially annealed (AZ31B-H24) [3]. In addition to texture weakening, the high bend formability, as demonstrated by repeated folding and flattening, has been reported in pure Mg when its grain size is reduced to about one micron and grain boundary sliding (GBS) becomes the dominant deformation mode. However, the exceptional formability by GBS is hitherto achieved only in pure Mg [30] and dilute binary alloy [31], and the samples have to be processed by high-pressure torsion [32] or extruded at a slower speed and a lower temperature [30] – both of which are considered anathema to process efficiency and thus difficult for up-scale production.

Recently, we have developed a sheet manufacturing process, which can produce thin sheets of Mg alloys by only one pass of large-strain flat extrusion and 1 – 3 passes of warm rolling (depending on sheet final thickness) with normal rolling speed (4.8 m/min) at an industrial scale. This has significantly shortened the long manufacturing process of Mg thin sheet by conventional multi-pass rolling, and thus named as "short-process" in this manuscript. Using this method, the fabricated Mg alloy sheets have high bend formability (Supplementary video 1). In this paper, the commercial AZ31 alloy, the most widely used Mg alloy composition, is taken as an example to demonstrate the appreciable ductility and outstanding bend formability of the sheet manufactured by this short process.

In general, any approach that could enhance the activity of deformation modes (dislocation slip and twinning) and their compatibility will increase ductility and formability. The widely used approaches include proper alloying addition, texture modification, and introduction of heterogeneous-grained and/or uniformly fine-grained microstructure. For example, dilute addition of Zn, Ca and rare-earth elements can reduce the stress required to activate pyramidal $\langle c + a \rangle$ dislocations [33–35] and weaken basal texture [36–39], which leads to much easier plastic deformation and higher formability. In addition to alloying addition, texture modification can also be realized by thermomechanical processing. For example, subjected to differential speed rolling, the (0002) pole is tilted away from the sheet normal direction (ND), and thus basal plane of most grains are no longer parallel to the RD and transverse direction (TD). The resultant higher activity of basal slip leads to better sheet ductility and formability than the conventionally rolled sheet [40–42]. Apart from tailoring grain orientations, the grain size and its distribution has significant effect on ductility. By grain refinement, the higher density of grain boundaries enhance the activity of $\langle c + a \rangle$ dislocations [43], accommodate and mediate local strain [44,45]. However, by collecting and analyzing the reported data about elongation and grain size [9], it is found that elongation has a weak correlation to grain size, and finer grains do not necessarily lead to higher ductility and formability, even for AZ31 alloy. It was also reported that grain size does not have a strong influence on relative activities of deformation modes when the grain size is above the micron scale [46,47]. Recently, it was reported that by inducing heterogeneous microstructure, i.e. mixture of large and small grains, the Mg-Al-based alloy will have higher strain hardening by dislocation pile-up at the boundaries between large and small grains, and enhanced activity of non-basal dislocation slip, and thus better ductility [48,49]. Via similar mechanism, the ductility enhancement was achieved by pre-compression of AZ31 plate along the TD, which introduce a high density of extension twins [50].

This approach, however, seems to be technically difficult for thin sheet.

In the present study, the outstanding bend formability in the short-processed AZ31 is achieved without adding calcium or rare earth elements that can weaken basal texture or enhance the activity of pyramidal $\langle c + a \rangle$ dislocations. Subjected to warm rolling, the AZ31 sheet should have typical strong basal texture, and no heterogeneous microstructure or twins were formed in the as-processed state. Under this circumstance, how to manipulate deformation modes to achieve higher ductility and bend formability without alternating alloy composition needs to be elucidated. To clarify the grain size effect, the deformation behavior of the short-processed AZ31 alloy developed in this study is investigated, and the ultra-fined-grained AZ31 extrusion developed in our previous study [51] is revisited as a comparison. Based on multiscale and complimentary *in-situ* characterization, an alternative interpretation is provided to explain the origin of high bend formability, allowing the key factors for dislocation slip operation in a strong-basal-textured Mg sheet to be discussed.

2. Experimental methods

2.1. Short processing of AZ31 sheet

The AZ31 billet, which was 156 mm in diameter and 250 mm in length, was extruded at the ram speed of 0.2 mm/s. Before extrusion, the billet and extrusion die was heated to 440 °C, and the billet container was heated to 350 °C. The extrusion ratio was 106, leading to a large true strain of 4.7 in extrusion. Despite the large strain, wear of the extrusion die is limited and 10 tonnes of AZ31 can be extruded before changing a new die. The as-extruded strip with a thickness of 1.5 mm was then further rolled to 0.5 mm by two passes. The thickness reduction per pass was 45%−70%. The rolling speed was 4.8 m/min. Before rolling Both the feedstock (extruded strip) and rolling wheelers were heated to 260 °C. The temperature of the rolling deformation area was monitored by infrared cameras to ensure the temperature was maintained between 210 and 260 °C.

2.2. Tensile and bending tests

For the tensile test, the specimens were metallographically prepared using SiC paper prior to each test, with a gage length of 10 mm and a width of 5 mm. Specimens of each condition were tested twice, with an initial strain rate of 0.001/s. Some of the tensile tests were interrupted at a strain of 0.08 and unloaded. The permanent changes in width and length were measured to determine the normal anisotropy, r. The r-value was obtained using the equation

$$r = \frac{\varepsilon_w}{\varepsilon_t} = \frac{\ln\left(w_f/w_i\right)}{-\ln\left(l_f/l_i\right) - \ln\left(w_f/w_i\right)} \tag{1}$$

where w, t, and l denote sample width, thickness, and length, respectively, and i and f denote initial and final values. The bend formability of the as-extruded and short-processed (extruded and warm-rolled) AZ31 sheet was tested using an Instron 4505 testing machine. The bend formability was assessed by a 3-point bending test, using punches with different diameters (D) from 0.2 mm to 14 mm. The gap between roller supports was adjustable and set equal to $D + 2$T. The punch displacement rate was 0.6 mm/min. The sample size for the bending test was 12 mm in length along the RD and 5 mm in width.

2.3. Finite element method simulation of bending process

The bending process was simulated by the FEM in LS-DYNA (Version 971, LSTC, Livermore, CA, Supplementary videos 2–5). In this model, five-layer solid elements were used to simulate the Mg alloy sheets. Belytschko-Tsay element was used to simulate the supports and punch. The material properties are shown in Table 1. The supports were fully constrained by the rigid material. The Mg alloy sheet in this model has a tensile-compressive yield asymmetric response. In the FEM, the punch adopts 'boundary_prescribed_motion_rigid' to set load conditions. The contact between the AZ31 plate and punch/die adopts a 'contact_automatic_nodes_to_surface' setup. The true stress-strain curve, which was calculated from the engineering strain-stress curve, was input into the material model to simulate the hardening behavior.

2.4. Digital image correlation (DIC)

The strain on the outer surface, which was simulated by FEM in bending, was validated by DIC. Because the DIC cameras could not fit into the die for bending, the bending strain was validated during the flattening of the bent samples. The samples, which were bent by 180° with a 4-mm diameter punch and by 90° with a 0.2-mm diameter punch, were painted with white color. Then, discrete black speckle patterns were sprayed for DIC characterization during flattening. In this work, a commercial stereo DIC system (ARAMIS® version 6.3) was used. The stereo system with left and right cameras allowed the out-of-plane position to be determined and, therefore, full 3D tracking of surface strain. The step size was set to be 5 pixels (95 μm) and the subset size was 15 by 15 pixels (285 μm) subsets [52].

2.5. In-situ *SEM and EBSD characterization*

An *in-situ* observation of bending test was conducted at room temperature using a screw-driven tensile stage placed inside a field emission scanning electron microscope (SEM, Zeiss Sigma 300) equipped with an EDAX-TSL EBSD system. The sample was bent at a constant displacement rate of 0.1 mm/min until 4.7 mm (the maximum displacement), then flattened by the reverse movement of the punch (Fig. 1). The support span was 26 mm, and the punch diameter was 5 mm. The *in-situ* bending process was simulated by FEM (Supplementary video 5) and the stress tensors of the outer and inner

Table 1
Material properties for finite element model.

Name	Materials model	Density (g/cm^3)	Young Elastic	Poisson's Ratio	Yield strength (MPa)
Mg AZ31 sheet	MAT_123	1.74	45	0.29	224
Supports and Punch	MAT_20	7.8	210	0.3	–

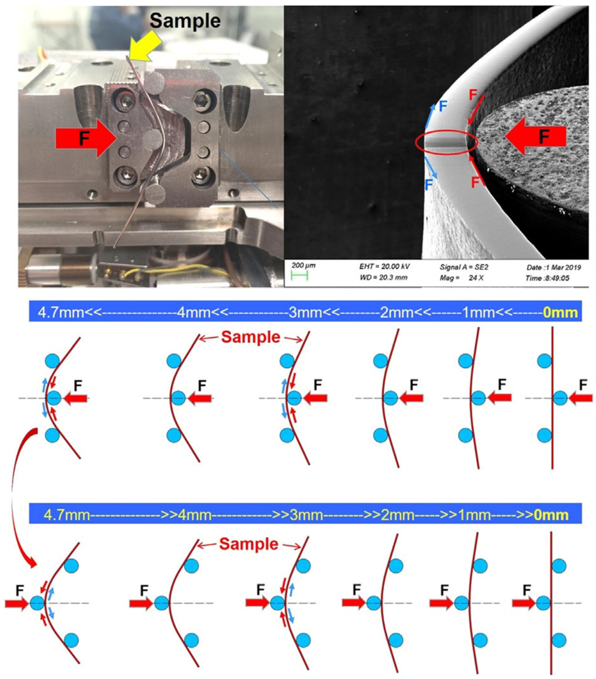

Dis.	Stress tensor of inner surface (in compression, MPa)	Stress tensor of outer surface (in tension, MPa)
0	$\begin{bmatrix}0&0&0\\0&0&0\\0&0&0\end{bmatrix}$	$\begin{bmatrix}0&0&0\\0&0&0\\0&0&0\end{bmatrix}$
1.0	$\begin{bmatrix}-5.0&-2.8&0\\-2.8&-185.1&-0.9\\0&-0.9&-64.0\end{bmatrix}$	$\begin{bmatrix}-0.1&-0.5&-0.1\\-0.5&179.3&0.8\\-0.1&0.8&60.8\end{bmatrix}$
2.0	$\begin{bmatrix}-10.6&-2.7&-0.4\\-2.7&-278.7&-1.1\\-0.4&-1.1&-124.5\end{bmatrix}$	$\begin{bmatrix}-0.1&-3.8&-0.1\\-3.8&269.2&1.1\\-0.1&1.1&116.4\end{bmatrix}$
3.0	$\begin{bmatrix}-15.1&0.1&0.2\\0.1&-285.3&-0.1\\0.2&-0.1&-148.2\end{bmatrix}$	$\begin{bmatrix}0.3&-7.6&0.6\\-7.6&270.1&0\\0.6&0&134.1\end{bmatrix}$
4.0	$\begin{bmatrix}-18.9&6.0&1.6\\6.0&-286.1&0.1\\1.6&0.1&-152.7\end{bmatrix}$	$\begin{bmatrix}0.2&-11.3&0.4\\-11.3&269.5&0\\0.4&0&135.1\end{bmatrix}$
4.7	$\begin{bmatrix}-22.1&8.4&0.3\\8.4&-291.7&0.1\\0.3&0.1&-157.2\end{bmatrix}$	$\begin{bmatrix}0&-16.5&0\\-16.5&268.2&-0.2\\0&-0.2&134.3\end{bmatrix}$

Fig. 1. Images and schematic illustrations showing the setup of bending and flattening process of *in-situ* EBSD observation. The stress tensor of the inner and outer surface in the *in-situ* bending test was obtained by FEM simulation. The input parameters for the FEM simulation are provided in Table 1.

surface as a function of punch displacement were obtained for calculating the generalized Schmid factor (GSF, details see Appendix 1). The RD-ND surface of the sheet was polished, using SiC paper, 50 nm diameter silica suspension, and subsequently ion polishing. For *in-situ* observation of tensile tests, the samples have a gage length of 4 mm and a width of 2 mm, and they were stretched with a cross-head moving speed of 0.1 mm/min. *In-situ* characterization was performed when the cross-head moved by 0.2 mm, 0.4 mm, 0.6 mm and 0.8 mm. The EBSD data was processed using TSL-OIM 8.

2.6. In-situ *TEM and STEM characterization*

In-situ TEM straining was carried out in a JEOL 2010HC microscope operated at 200 kV, using a Gatan room-temperature straining holder. MEGAVIEW III CCD camera was used to record microstructural evolution (Supplementary video 6). The TEM results were analyzed using a Pycotem package [53]. STEM and STEM-EDXS characterizations were performed in an FEI F20 transmission electron microscope equipped with a Bruker XFlash 6TI30 EDX detector. The STEM-EDXS data were analyzed using the software Esprit 2.0. The samples were prepared by electric discharge cutting, followed by mechanical grinding to 50 µm thick using 4000 grid SiC sandpaper. The samples were then ion-polished using Gatan Precision Ion Polishing System (voltage 4.8 kV and angle 4°) at −100 °C until a small hole formed in the specimen.

2.7. *X-ray diffraction*

The X-Ray diffraction profiles are measured using a Bruker D8 advanced X-ray diffractometer equipped with a Cu-Kα beam source and a high throughput LynxEYE 1-dimensional detector. The 1-D diffraction spectrum was obtained using a scan rate of 1 s/step, a step size of 0.01°, and a scanning range between 30 and 70° at 40 kV and 40 mA. Zero error and instrument profiles are assessed based on the scan of the standard reference material (SRM 660, LaB_6) from the National Institute of Standards and Technology.

3. Results

3.1. *Microstructure characterization*

Fig. 2a–c show significant difference in microstructure and texture at the different parts of the as-extruded strip. At the edge part, the 1.5 mm-thick strip has coarse grains and a typical extrusion texture, i.e. the c-axis of grains is perpendicular to the extrusion direction (ED). At the ¼ to edge part, fine

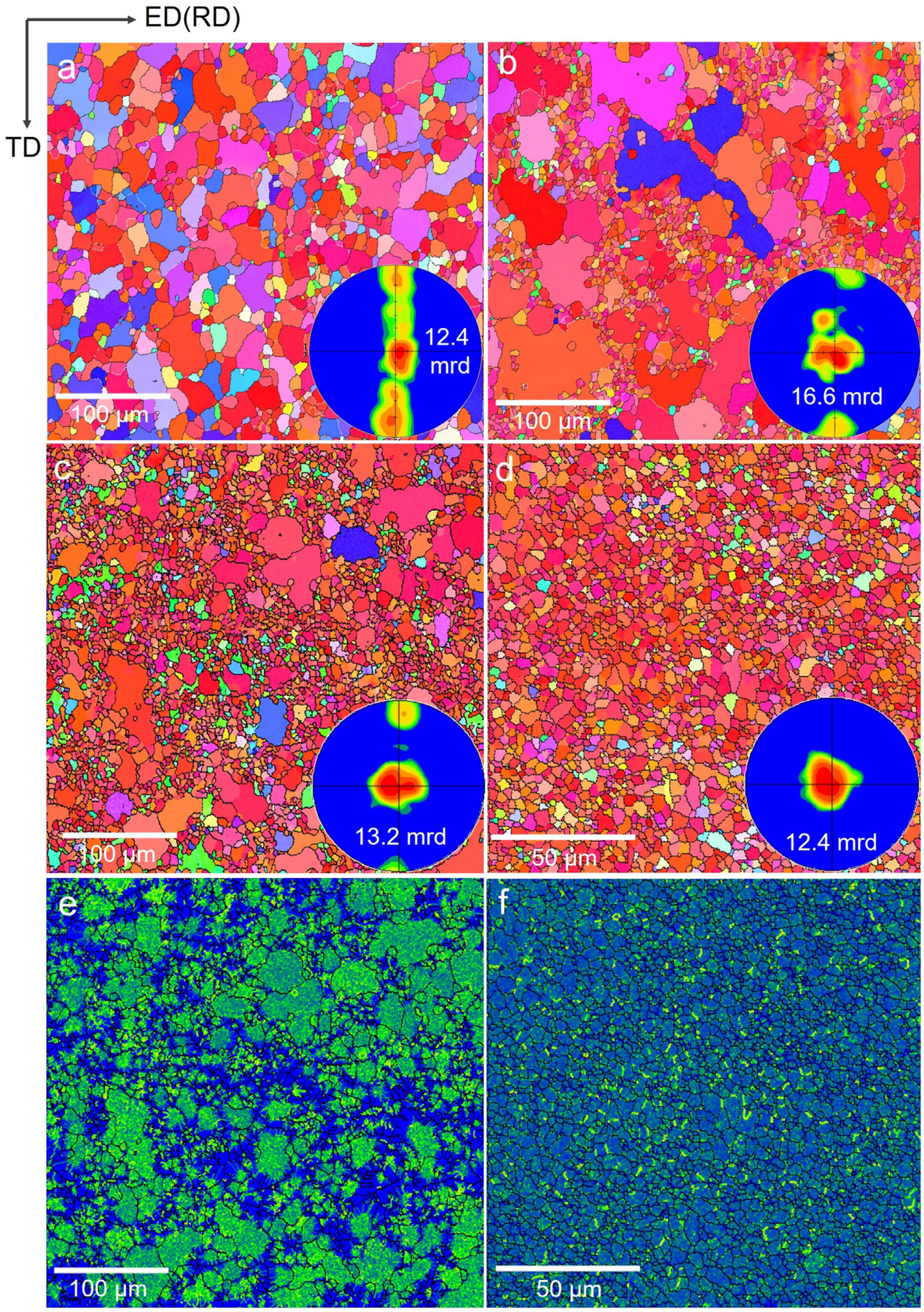

Fig. 2. (a–d) EBSD orientation maps and corresponding (0002) pole figures of the (a) edge, (b) ¼ to edge, (c) center part of as-extruded strip and (d) short-processed sheet from their ED(RD)-TD face. (e, f) KAM maps of the center part of as-extruded strip and short-processed sheet.

grains appear between coarse grains. The sheet basal texture, i.e. the c-axis of grains parallel to the sheet's normal direction (ND), becomes more significant. At the center part, the fraction of fine-grains increases, and it shows a typical bimodal microstructure. The average grain size was 16 μm in diameter, but there are ~15% of grains with a diameter larger than 30 μm. The (0002) pole figure shows two distinctive texture components, i.e. [0001]//ND and [0001]//transverse direction (TD). In contrast, after further warm rolling, the short-processed sheet has uniform microstructure and texture. The fine and equiaxed grains with an average size of ~4.8 μm in diameter, as shown in Fig. 2d, are representative of different parts of the short-processed sheet. The short-processed AZ31 sheet has a strong basal texture of 12.4 mrd (multiples of random distribution). The kernel average misorientation (KAM) maps show that the as-extruded strip is composed of fine recrystallized and large deformed grains (Fig. 2e) but the short-process sheet is recrystallized with low and uniform strain (Fig. 2f). The grain orientation spread (GOS) of the short-processed AZ31 is 0.75° in average. Considering that a

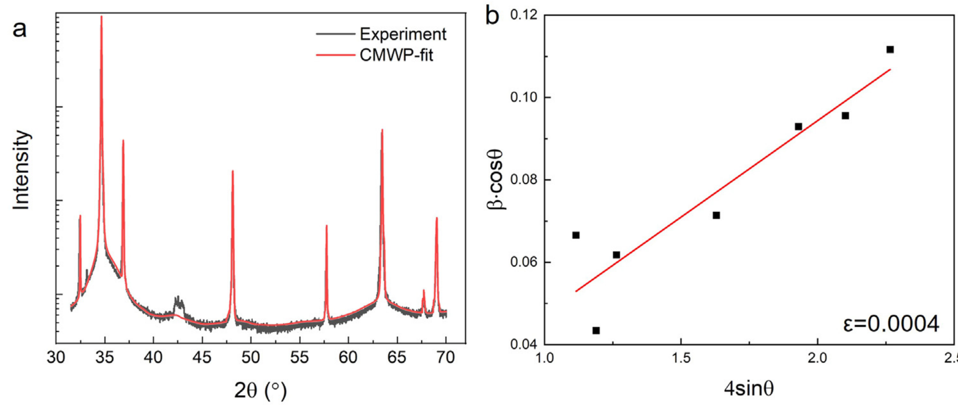

Fig. 3. (a) experimental measured and CMWP-fit XRD spectra of the short-processed AZ31 sheet and (b) calculation of micro-strain based on the peak broadening using the Williamson–Hall method.

GOS value of less than 1°–2° is a criterion for identifying recrystallized grains [54,55], the short-processed AZ31 sheet is recrystallized.

In order to support the low residual strain in the fully recrystallized microstructure, XRD is performed. Based on the spectrum (Fig. 3a), the microstrain can be obtained from the XRD spectrum based on the peak broadening using the Williamson–Hall method [56],

$$\frac{\beta\cos\theta}{\lambda} = \frac{1}{D} + 2\varepsilon\left(\frac{2\sin\theta}{\lambda}\right) \tag{2}$$

where ε is the microstrain, D is the domain size, θ is the angle between the incident beam and sample, and λ is the wavelength (=0.154 nm for Cu Kα). By fitting the peak broadening, the microstrain of the short-processed AZ31 is calculated to be 0.004 (Fig. 3b). In order to estimate the dislocation density, an extended convolutional multiple-whole-profile (e-CMWP) method is used, in combination with the Levenbery–Marquardt peak-fitting procedure and Monte Carlo statistical method [57–59] (Fig. 3a). This method has proven to be powerful for the quantitative characterization of lattice defects in crystalline materials [60–62], and the computer program CMWP-Fit has been developed by Ungár et al. [63]. The input information includes the experimental XRD spectrum, diffraction peak index, instrumental file, lattice type and parameter of AZ31, and the contrast factor. In this work, 8 diffraction peaks, including $\{10\bar{1}0\}$, (0001), $\{10\bar{1}1\}$, $\{10\bar{1}2\}$, $\{11\bar{2}0\}$, $\{10\bar{1}3\}$, $\{10\bar{2}2\}$, $\{20\bar{2}3\}$, were used for e-CMWP fitting. The instrumental file was obtained using SRM 660 LaB_6 from the National Institute of Standards and Technology and input to the program to correct the instrumental broadening effect in the XRD pattern. The contrast factor is the averaged value of the most popular ⟨a⟩-type dislocations, including ⟨a⟩-type edge dislocations on basal and prismatic planes, and ⟨a⟩-type screw dislocation on the prismatic planes, based on the assumption that the dislocations with a c-component and $\langle c + a\rangle$-component were marginal. The value of the contrast factor for each dislocation type is provided in the literature [64]. Via the e-CMWP fitting and iteration procedure, the overall value of dislocation density was determined as $\sim 5 \times 10^{13}$ m^{-2}. The low value of dislocation density measured by XRD is consistent to the EBSD characterization.

3.2. Tensile properties and bend formability

Fig. 4 shows that different parts of as-extruded AZ31 have different ductility. Although their 0.2% proof strengths are similar about 198±4 MPa, the edge part has the lowest elongation of 11%. The ¼ to edge part has a higher elongation of 16% whilst the total elongation of the center part is 17%. After further warm rolling down to 0.5 mm thick, the 0.2% proof strength and elongation increased simultaneously to 224±5 MPa and 27±2%, when specimens from different parts of short-processed sheets were tested. The strength-ductility combination of the short-processed AZ31 sheet is outstanding among Mg-Al-Zn alloys [9,65]. The short-processed AZ31 sheet has higher work hardening exponent (0.16) and normal anisotropy (2.03) than the as-extruded strip (Table 2).

Regarding bend formability, the 1.5-mm thick as-extruded strip can be bent with a 10 mm-diameter punch in the 90° cold bending test, resulting in a bend radius of 3.3T. Although the bent sample was not fractured, some tiny defects were observed on the outer surface of the bent AZ31 strip (Fig. 5a). The strain during bending was calculated using FEM. Because bend forming is affected by bend radius, angle and sheet thickness [8], the quantification of the bending strain allows the comparison of deformation state between the sheets that have different thicknesses, and that are bent with different radii to different angles. The maximum strain of as-extruded strip in the 90° cold bending test is ∼ 0.175.

After further warm-rolling, the short-processed AZ31 sheet can be bent without cracking or surface defect in the 90° bending test using a punch with a diameter of 0.2 mm, resulting in a bend radius of 0.2T (Fig. 5b). The FEM simulation shows a higher true strain at the bent section, about 0.25 on the inner surface and 0.28 on the outer surface. The difference in true strain between the inner and outer surfaces is likely caused by plastic anisotropy in Mg alloys. Furthermore, the short-processed AZ31 sheet can be repeatedly bent with

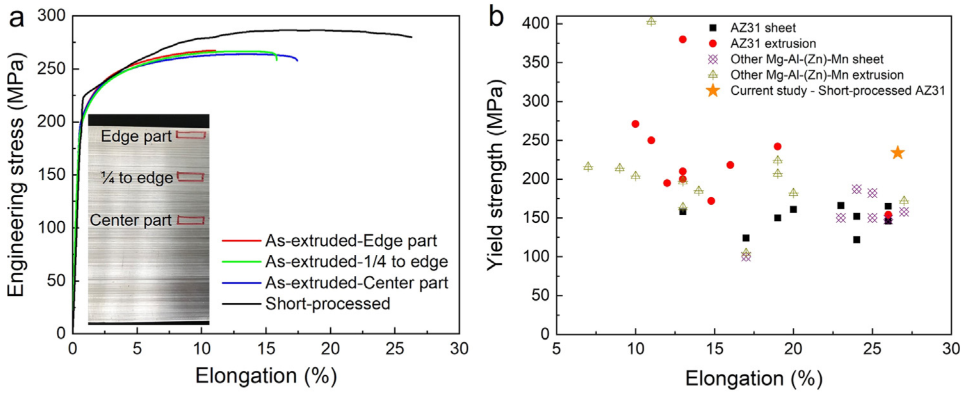

Fig. 4. (a) Engineering stress-strain curves of the as-extruded strip and short-processed sheet. Photo inset shows the edge part, ¼ to edge, and center part of as-extruded strip. (b) Comparison of the tensile property with those of AZ-based alloys reported by literature [9,65].

Table 2
Tensile properties and normal anisotropy of as-extruded strip and short-processed sheet.

Sample	YS (MPa)	UTS (MPa)	Total El. (%)	Strain hardening exp. (n)	Normal anisotropy (*r*)
As-extruded-Edge part	202	268	11	0.12	0.51
As-extruded-¼ to edge	198	267	16	0.13	0.54
As-extruded-Center part	195	264	17	0.13	0.62
Short-processed	224	288	27	0.16	2.03

a 4 mm-diameter punch, i.e. bent by 180°, flattened, and then reversely bent without any visible cracks (Fig. 5c). Photos in Fig. 5 show observable springback after the bent sample was unloaded, as springback caused by elastic recovery can be as much as 30° for a 90° bend in cold forming of Mg alloys [3]. FEM simulation reveals the maximum strain of ∼0.13 bent with a radius of 4T up to 180° By comparing with the minimum bend radii of the Mg alloy sheet reported in the literature (Fig. 5d), it is found that the bend radius of 0.2T in this study is nearly ten times lower than the bend radius reported for Mg alloy sheet. The lowest bend radius reported (including rolled sheet and extruded strip of Mg alloys) is 1.9T for 90° cold bending [3,28]. The bend radius of 0.2T is also close to the bend radii of O-tempered Al alloy sheets in the 90° cold bending test [8]. To validate the bent strain simulated by FEM, the outer surface of the bent area was speckled and the bent specimens were pulled until flattened. Using DIC, the total strain during flattening was measured to be 0.285 and 0.133 for the 90° bent sample (0.2T) and 180° bent sample (4T), respectively (Fig. 5e). The values of total strain during flattening (measured by DIC) are similar to strain during bending (simulated by FEM).

In summary, the microstructural observation and tensile and bending tests suggest that appreciable ductility and high bend formability can be achieved in conventional Mg sheet alloy even though it possesses a strong basal texture. The mechanism is explored in the following sections.

3.3. In-situ *observation of microstructure evolution during bending*

To reveal the origin of the high bend formability, the microstructure evolution of the short-processed AZ31 sheet during bending and flattening was characterized using *in-situ* EBSD. In the tensile region during bending (Fig. 6a–d), the microstructural change can hardly be distinguished from orientation maps (Fig. 6a and c), but the increase in GOS suggests the plastic deformation in the tensile region (Fig. 6b and d). In the compression region, twin bands form, propagate and intersect with the increasing bending (Fig. 6a and c). The area fraction of twins in the compression region was 17.5% after the punch moved by 4.7 mm (equivalent to 0.043 true strain at the surface, Fig. 6i). During bending, the averaged GOS value of the whole observed area was increased from 0.75° to 0.95° (Fig. 6j). During flattening, the compressive region is subjected to a tensile load, leading to the detwinning in the compressive regions (Fig. 6e–h). Once the sample is fully flattened, the twins disappear from the region that was originally under compressive strain (Fig. 6g).

The twinning and detwinning during bending and flattening were examined at higher magnification. It is found that the plastic deformation is highly heterogeneous in the compression region, as demonstrated by the higher GOS along the twin bands (Fig. 7a and b). The twins observed are predominantly with equiaxed shape, suggesting that once the twins are formed, they thicken, grow, and replace their parent grains. Taking advantage of *in-situ* EBSD characterization, each pair of twin-parent grain can be identified (Fig. 7c–k). By analyzing their orientation relationship, the observed twins are inevitably $\{10\bar{1}2\}$ extension twins. The $\{10\bar{1}1\}$ contraction twinning or $\{10\bar{1}1\}$-$\{10\bar{1}2\}$ double twinning, which might cause micro-cracking [66,67], was not observed. During flattening, detwinning occurs and GOS is decreased in the detwinned grains (Fig. 7l–n). Accompanied by detwinning, the twin boundary may act as a dislocation sink to absorb dislocations [68]. The detwinning alleviates the local high strain

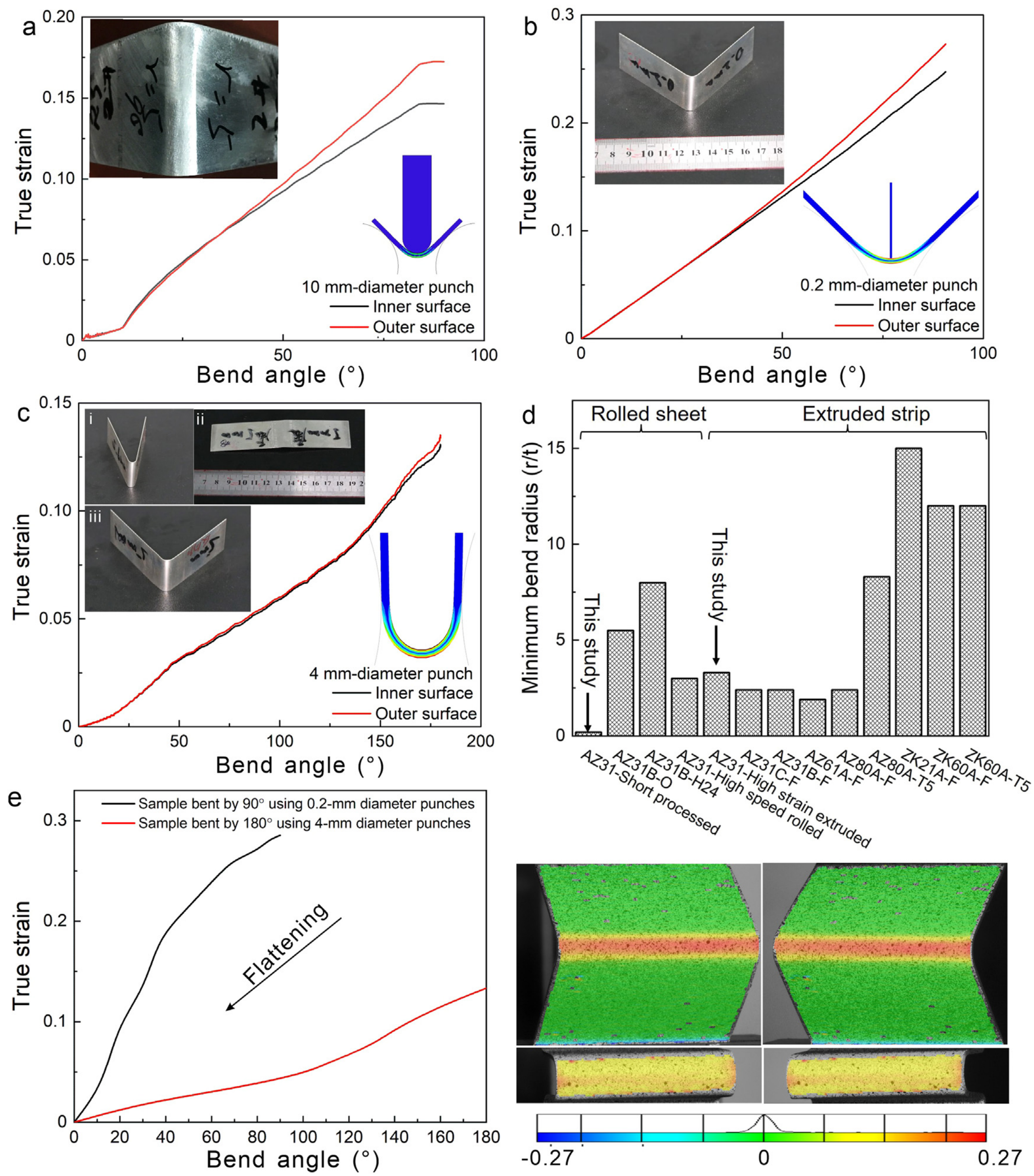

Fig. 5. True strain at the outer and inner surfaces as a function of bend angle, when (a) the 1.5 mm thick as-extruded strip was bent by 90° with 10-mm diameter punch, and when the 0.5 mm thick short-processed sheet was bent by (b) 90° and (c) 180° with 0.2-mm and 4-mm diameter punches, respectively. Photo inset in (a, b) shows that the sheet was successfully bent by 90° with 3.3T and 0.2T bend radius, and photos in (c) show that the sheet was (i) bent by ~180°, (ii) followed by flattening, and (iii) reverse bending by ~90° without any visible crack. The bent specimens were spring-backed after being removed from the testing rig. (d) Minimum bend radii of rolled sheet and extruded strip in this study and reported by literature, whose thicknesses are in the range between 0.5 and 6.3 mm [3,28]. These samples were bent by 90° at room temperature. (e) DIC result of strain evolution during flattening of short-processed samples, which were previously bent by 90° and 180° with 0.2-mm and 4-mm diameter punches, respectively. Photos in (e) are from the left and right cameras of bent and speckled sample, which are superimposed with the strain map before flattening.

associated with the twin bands and leads to a much slower increase in strain during flattening than during bending (Fig. 6j). The resultant uniform distribution of strain (Fig. 6f and h) allows the possibility of further repeated bending.

In the SEM image of the sample bent at 4.7 mm punch position, the plastic deformation zones by tensile and compressive strain can be clearly identified (Fig. 8a). In any bending process, there must be a neutral line where the strain along this line should be zero. However, the neutral line is not necessarily in the middle of the sample thickness. To identify the neutral line position, FEM is used to simulate the bending process. It is found that the neutral line is slightly shifted towards to tensile region by ~30 μm towards the tensile region. This is consistent with the GOS mapping and distribution. The plastic-deformed region was then segmented into 7 areas (labeled A–G). For identifying the deformation mode

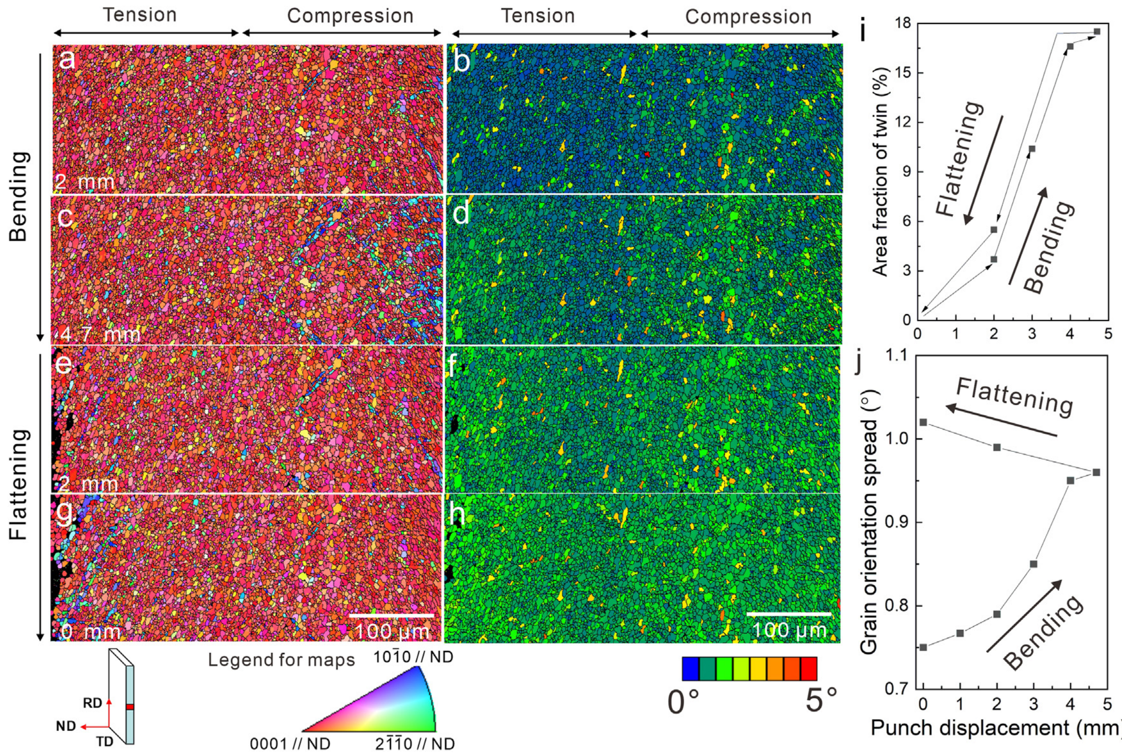

Fig. 6. Microstructure and strain evolution during bending and flattening. (a–h) *in-situ* EBSD orientations map and corresponding grain orientation spread map (GOS) of sample RD-ND surface in bending as the punch moved from (a, b) 2 mm to (c, d) 4.7 mm in bending, and then moves back to (e, f) 2 mm and (g, h) the original position in flattening. (i) Area fraction of twins in the compressive region and (j) GOS as a function of punch displacement during bending and flattening.

between the outer and inner surface, IGMA is used to analyze the deformation mode of each areas. Based on EBSD results, the in-grain misorientation analysis (IGMA) method was used to identify the slip mode of Mg alloys [54,55,69]. The peak intensities of misorientation axes can be around the ⟨0001⟩ (⟨0001⟩-type distribution), ⟨uvt0⟩ (⟨uvt0⟩-type distribution), and in a uniform distribution or with multiple peaks [69]. The result is shown in Fig. 8b, it can be found that for the areas close to the outer and inner surface (areas A and G) where the strain is higher, the IGMA distribution is closer to the ⟨0001⟩-type, indicating the significant operation of prismatic slip. When it is closer to the neutral line, the IGMA distribution becomes uniform or even ⟨uvt0⟩-type, indicating the enhanced operation of basal dislocation slip.

To further reveal the deformation modes in the tension region, six grains were selected from the near outer surface as representatives. Their microstructural evolution during bending (Fig. 9a–d), was examined at higher magnification. Grains G1–G6 are elongated and rotated up to 4°– 6° during bending (Fig. 9e). When the sample was bent as the punch moved to the 2-mm position (Fig. 9f), it is apparent that G6 has a ⟨0001⟩-type distribution, indicating the dominant activation of prismatic ⟨a⟩ slip. Grains G3 and G5 have nearly ⟨uvt0⟩-type distribution. Both basal ⟨a⟩ slip and second-order pyramidal $\langle c + a\rangle$ slip can lead to ⟨uvt0⟩-type distribution. Considering the critical resolved shear stress (CRSS) of pyramidal slip is significantly higher than the basal slip [9], it is reasonable to speculate that the dominant slip mode for ⟨uvt0⟩-type distribution in Grains G3 and G5 is basal ⟨a⟩ slip. Grains G1, G2, and G4 have uniform IGMA distribution, indicating there are no dominant slip modes of these grains. Thus, the deformation of G1, G2, and G4 in bending is likely to be accommodated by the co-activation of basal and prismatic slip modes up to the 2-mm punch position.

During further bending to the 4.7-mm punch position, the grain rotation and the change of stress state (Fig. 1) have changed the generalized Schmid factor (GSF) values, which is now widely adopted to evaluate the resolved shear stress for various slip systems under multi-axial stress state, including bending [70]. As a result, the slip modes of some grains will be changed during further bending (Fig. 9g and Table 3). For example, the GSF ratio between prismatic and basal slip (m_{prism}/m_{basal}) decreases from 1.7 to 1.4 in Grain G2 with the punch moving from the 2-mm to 4.7-mm position. The decreased m_{prism}/m_{basal} ratio may cause a higher activity of basal slip and thus the change of IGMA type from a uniform distribution to ⟨uvt0⟩-type. In contrast, the m_{prism}/m_{basal} ratio increases from 2.3 to 3.5 for G1 and from 1.3 to 1.6 for G5, when the punch moved from the 2-mm to 4.7-mm position. The increased m_{prism}/m_{basal} ratio suggests an easier operation of prismatic slip. This is consistent with the IGMA observation, i.e. the increase of the intensity around ⟨0001⟩ in Grain G1 and the change of IGMA type from the ⟨uvt0⟩-type to a uniform type in Grain G5. Based on the analysis of Grains G1–G6 (Table 3), it is found that the m_{prism}/m_{basal} ratio is always lower than 1.6 when basal slip is dominant and pris-

Please cite this article as: S. Xu, P. Xiao, X. Wu et al., Mechanistic investigation of highly bendable magnesium alloy sheet fabricated by short-process manufacturing, Journal of Magnesium and Alloys, https://doi.org/10.1016/j.jma.2023.09.026

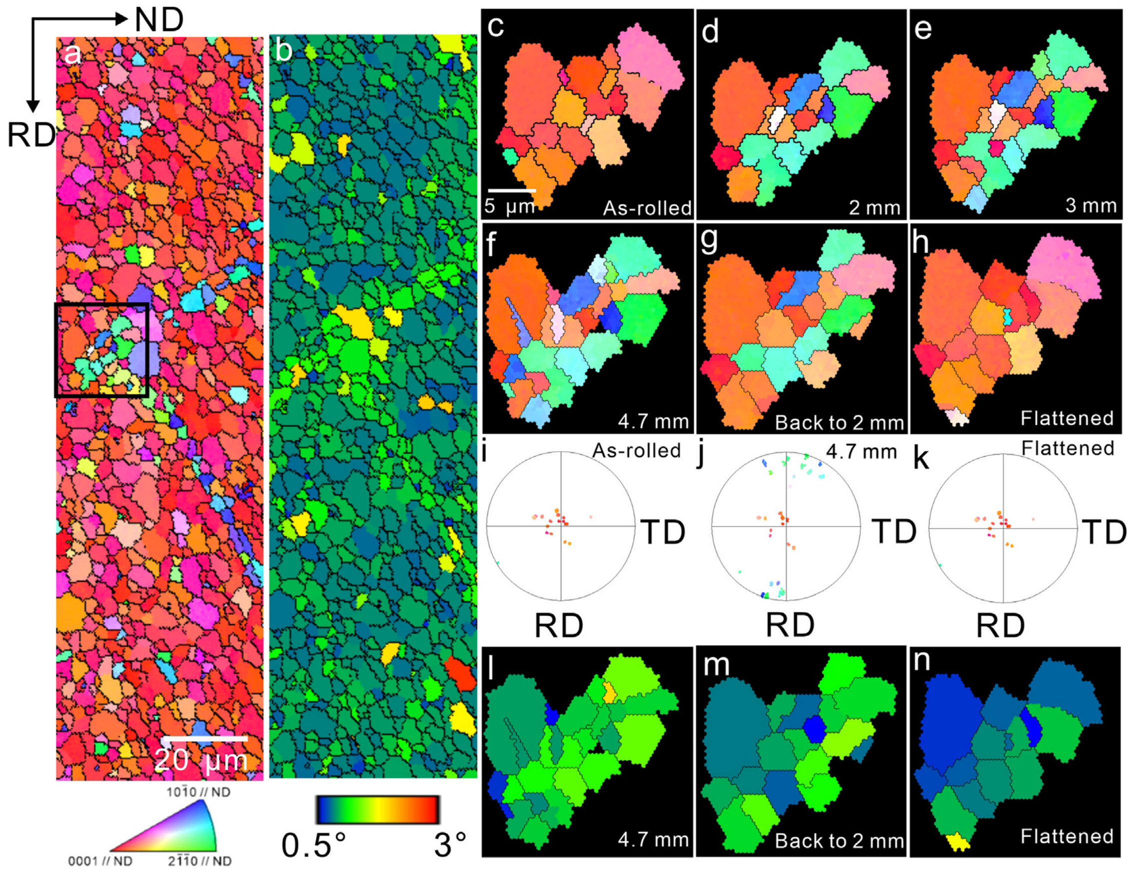

Fig. 7. (a, b) EBSD orientation and GOS maps show the intersection of twin bands and the localised strain along the twin bands of the bent AZ31 sheet. *In-situ* EBSD orientation maps show (c–f) twinning during bending and (f–h) detwinning during flattening. (i–k) (0001) pole figure shows the orientation of grains and twins (i) in the as-rolled state, (j) bent with 4.7 mm punch position, (k) after flattened. (l–n) *In-situ* GOS maps show the decrease in GOS level associated with detwinning during flattening from the 4.7 mm punch position to the original position.

Table 3
Generalized Schmid factor (*m*) and IGMA type of the six grains in Fig. 9 in the as-rolled state and at the 4.7-mm punch position.

Grains	2mm				4.7mm			
	basal	prism.	m_{prism}/m_{basal}	IGMA type	basal	prism.	m_{prism}/m_{basal}	IGMA type
G1	0.21	0.39	2.3	Uniform	0.16	0.54	3.5	⟨0001⟩
G2	0.26	0.43	1.7	Uniform	0.30	0.43	1.4	⟨uvt0⟩
G3	0.31	0.45	1.4	⟨uvt0⟩	0.30	0.43	1.4	⟨uvt0⟩
G4	0.23	0.50	2.2	Uniform	0.23	0.51	2.2	Uniform
G5	0.33	0.42	1.3	⟨uvt0⟩	0.26	0.42	1.6	Uniform
G6	0.09	0.50	5.5	⟨0001⟩	0.10	0.52	5.2	⟨0001⟩

matic slip is suppressed (⟨uvt0⟩-type distribution). Otherwise, a uniform or ⟨0001⟩-type distribution of the in-grain misorientation axis occurs, suggesting that prismatic slip is activated. Because the CRSS ratio between prismatic and basal slips should be equal to the m_{prism}/m_{basal} ratio [71,72], the $CRSS_{prism}/CRSS_{basal}$ is estimated at ∼1.6.

To obtain a more reliable estimation of slip modes in bending, 100 grains, randomly selected from the tensile region, were examined using the IGMA method. Among these 100 grains, 43 grains are predominantly deformed by basal slip as they are with ⟨uvt0⟩-type distribution, whilst 22 grains are predominantly deformed by prismatic slip with ⟨0001⟩-type distribution. The remaining 35 grains have uniform IGMA distribution, thus they are likely to be deformed by both basal and prismatic slip modes. The m_{basal} and m_{prism}/m_{basal} of these 100 grains are shown in Fig. 9h. It is found that the prismatic-slip dominant grains have high m_{prism}/m_{basal} > 4.6. As a comparison, the basal-slip dominant grains had low m_{prism}/m_{basal} <∼1.5. Therefore, the examination of a large set of grains shows that the $CRSS_{prism}/CRSS_{basal}$ is close to 1.5.

3.4. *Deformation mode analysis through* in-situ *characterization of tensile test*

Because the maximum strain that can be achieved in the *in-situ* bending test is limited, the short-processed sheet was de-

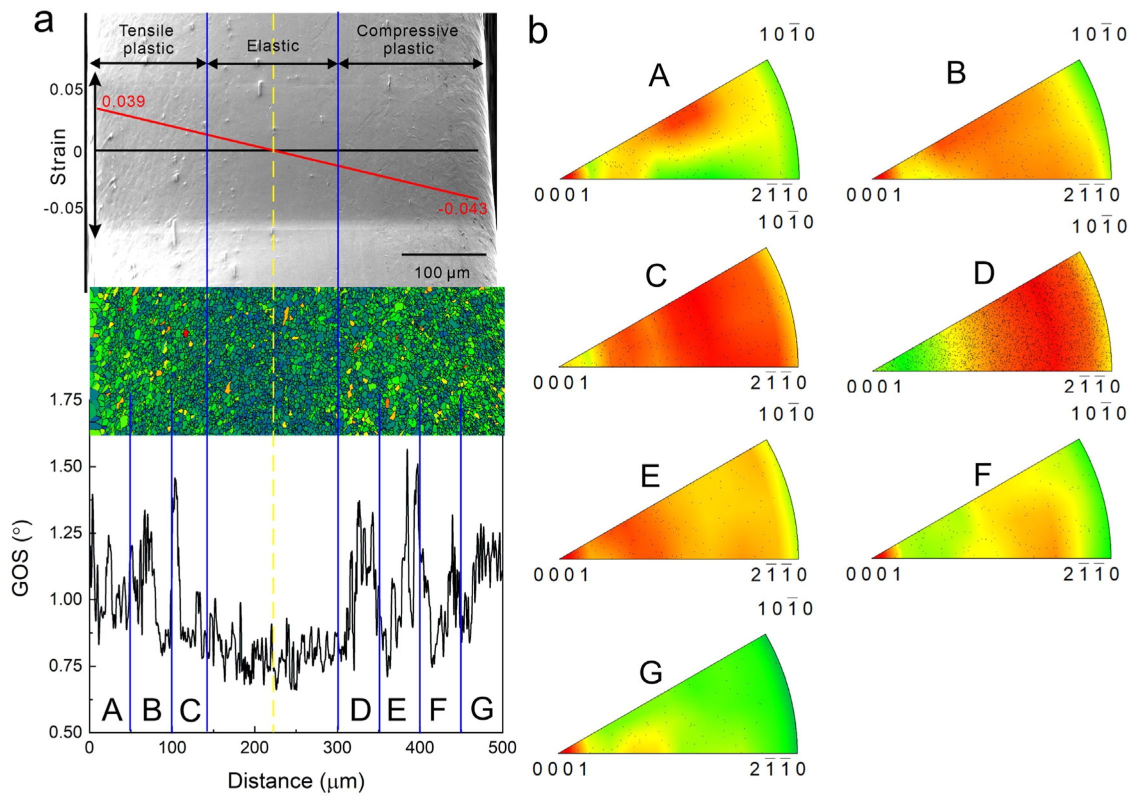

Fig. 8. (a) SEM image of the sample side surface after it was bent as the punch moved to the 4.7 mm position. The tensile and compressive plastic deformed regions and the elastic deformed region can be distinguished. The true strain distribution, from 0.039 on the outer surface to −0.043 on the inner surface, was calculated by FEM and illustrated. The neutral line is shown by the yellow dashed line, which is shifted toward the tensile region. Based on the grain orientation spread (GOS) map, the plastic deformed regions are segmented into 7 areas (labelled A-G), with a width of ∼50 um for each area. The GOS of 7 plastic deformed areas and the elastic deformed area is provided. (b) In-grain misorientation axis (IGMA) analysis of the areas A–G.

formed by a larger strain via an *in-situ* tensile test (Fig. 10a–h). The crosshead of the tester has moved by 10%, 15%, and 20% in terms of specimen gage length. However, by tracking the surface features (blue arrows in Fig. 10a and e), the actual elongation of the observed sample area is lower than the sample elongation measured by the cross-head. At 20% sample elongation, the observed surface areas are elongated by 13.6% and 10.0% for the short-processed and as-extruded samples, respectively. By measuring the reduction of white rectangles along the TD, the *r*-value can be calculated. The *r*-values measured from *in-situ* observation method is about 2.13–2.22 and 0.55–0.69 for the short-processed sample and as-extruded sample, respectively. Similar to the measurements from the *ex-situ* mechanical tests, the *r*-value of the short-processed sample is much higher than that of the as-extruded sample.

The surface observation also shows that the short-processed AZ31 sample has a much more uniform deformation than its as-extruded counterpart. As demonstrated by Fig. 10i and j, in the as-extruded AZ31 sample, the deformed Grains I and II have much larger sizes than the surrounding fine recrystallized grains. Based on the *in-situ* observation (Fig. 10k and l), the deformation among the recrystallized grains (highlighted by the white rectangles) is more significant than the deformed Grains I and II. Fig. 10l shows highly localized deformation between them (highlighted by the yellow arrow) and in-grain cracking in Grain I (highlighted by the red arrow). Such a strain localization may be caused by the limited capability of plastic deformation of Grains I and II, and eventually becomes a shear band, which contains arrays of in-grain cracks, throughout the TD (Fig. 10m).

To reveal the deformation mode of the short-processed AZ31 sample, slip trace analysis was performed. Based on the EBSD result, the three Euler angles of particular grains selected from EBSD map can be obtained and input in the MATLAB code for slip trace analysis. By comparing the orientation of a selected trace with the 12 potential traces, which correspond to different slip systems. A detailed introduction to this method has been provided in Appendix 2 and the literature [73,74]. In the *in-situ* tensile test, slip traces are predominantly found in the grains with a relatively high m_{basal} value (>0.3), and slip traces observed in these grains are identified to be basal slip traces (Fig. 11).

The non-basal-oriented grains, where slip traces can be observed, however, only take a small fraction of total grains. For the majority of grains, the slip traces are not observed but these grains are still significantly deformed. Fig. 12 shows a local area containing grains numbered 1–10, and this area was elongated by 16.2% (by tracking the surface features). Whilst

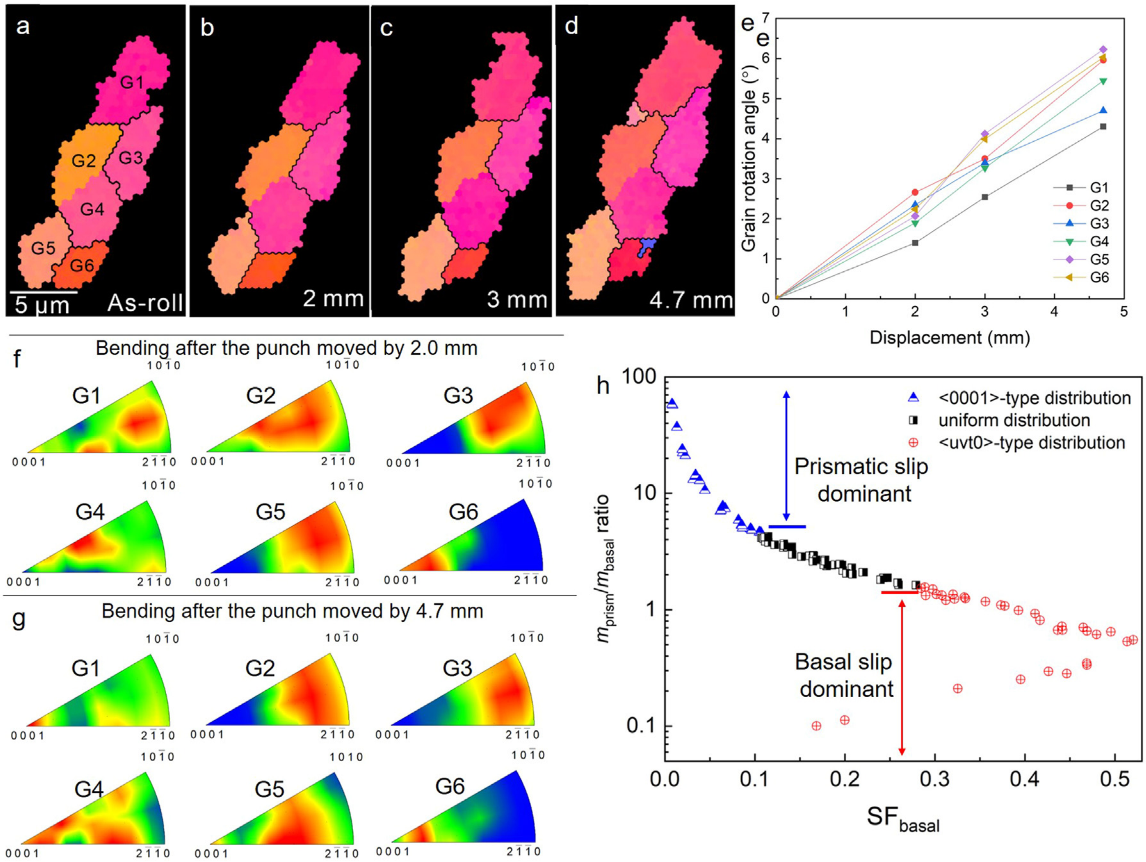

Fig. 9. (a–d) *In-situ* EBSD orientation maps of selected Grains G1–G6 in the tensile region during bending to 4.7-mm punch displacement. (e) Grain rotation angle of six selected grains as a function of punch position during bending. (f, g) Inverse pole figures showing IGMA distributions of each grain after bending to the (f) 2-mm and (g) 4.7-mm punch position. (h) The IGMA types, m_{basal}, and m_{prism}/m_{basal} of 100 randomly selected grains from the tensile region after bending to the 4.7-mm punch position.

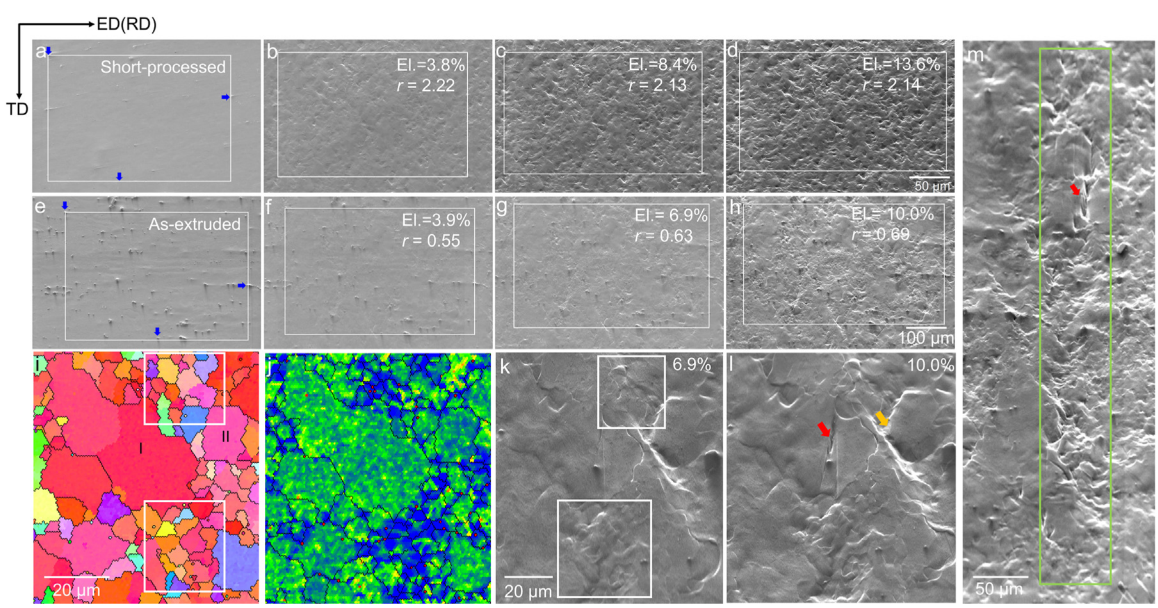

Fig. 10. *In-situ* SEM observations of (a–d) short-processed and (e–h) as-extruded AZ31 samples when the crosshead of the tester has moved by (a, e) 0%, (b, e) 10%, (e, f) 15%, and (d, h) 20% in terms of specimen gage length. Surface features highlighted by the blue arrows were used to track the same area (highlighted by white rectangles). (i–l) Observation of as-extruded AZ31 during tensile tests at higher magnification. (i) EBSD orientation map, (j) corresponding KAM map, and (k, l) SEM images at 6.9%, and 10.0% elongation of a local area. White rectangles highlight recrystallized grains adjacent to deformed Grains I and II. Red and yellow arrows in (l) highlight an in-grain crack in grain I and severe deformation between grains I and II, respectively. (m) localized strain and cracking along the TD at 10.0% elongations of as-extruded AZ31 (highlighted by green rectangle).

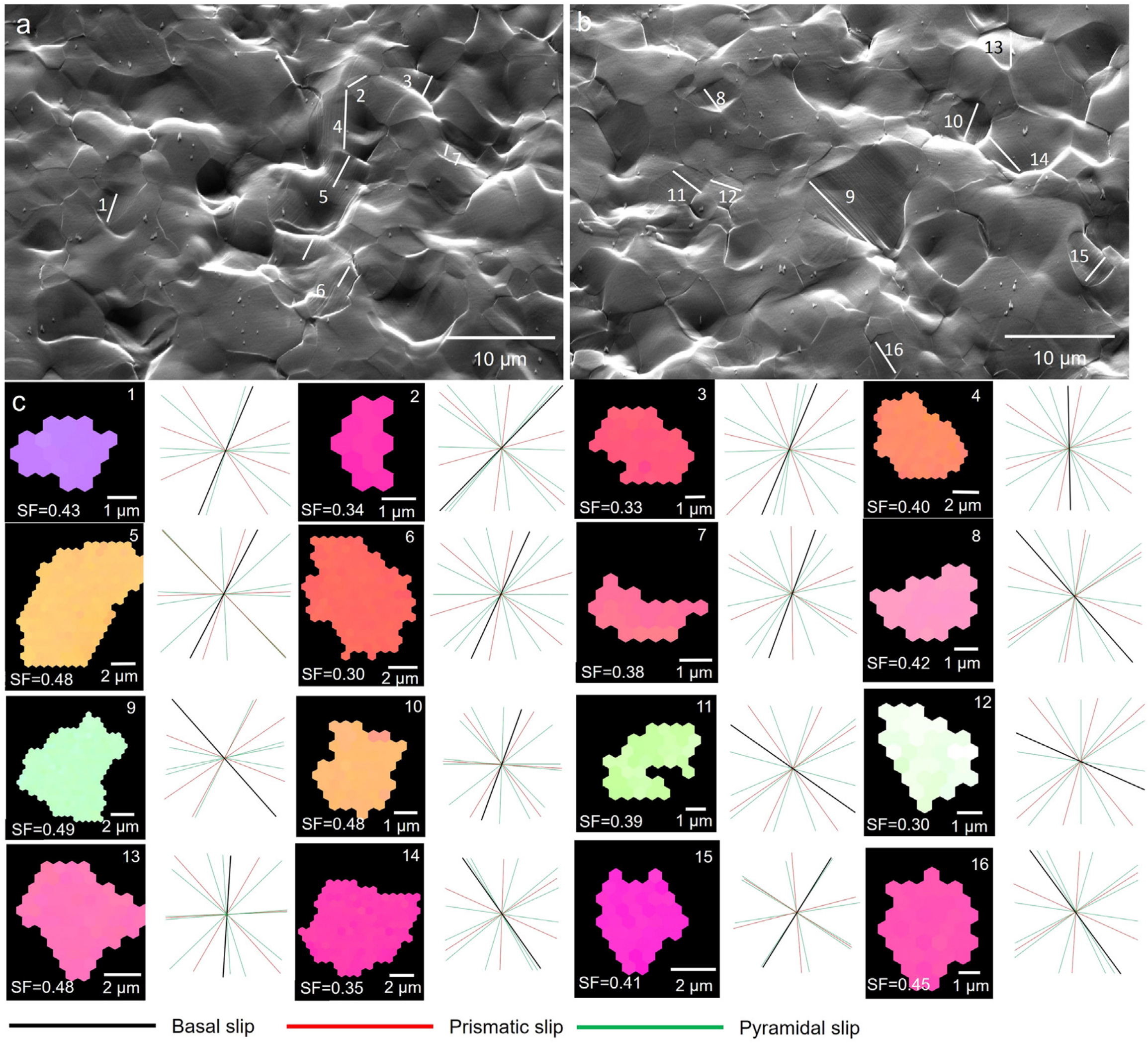

Fig. 11. (a, b) Two SEM images of the short-processed AZ31 after it is elongated by 13.6% in SEM *in-situ* tensile stage. (c) EBSD orientation map of 16 grains in which slip traces were identified. Based on their orientations, the trace direction of basal slip, prismatic slip (3 variants) and pyramidal II slip (6 variants) can be obtained. By matching the potential slip traces with those observed in the SEM image, the slip traces are identified to be basal slip traces.

only a few weak traces for basal slip can be observed in Grain 1 (with a tilt angle of 35° to the ND and a high m_{basal} value of 0.42), no slip trace can be observed in Grains 2–10 (whose tilt angle to the ND are within 20°). Apparently, Grains 2–10 are also plastically deformed. To reveal the deformation mode of these grains, the IGMA was used and it is shown that Grain 1 has a high intensity of misorientation axis around $\langle 10\bar{1}0\rangle$, indicating the dominant operation of basal slip. As a comparison, Grains 2–6 have a uniform distribution of misorientation axis, indicating that both basal and prismatic slips are operative. In contrast, Grains 7–10 have typical $\langle 0001\rangle$-type distribution, indicating the dominant operation of prismatic slip. The m_{prism}/m_{basal} ratios for Grains 1, 2–6, and 7–10 are 0.9, 1.6–3.3, and 4.2–14.7, respectively (Table 4). Therefore, similar to the analysis through *in-situ* bending test observations, the deformation mode analysis via *in-situ* tensile test also suggests that prismatic slip should be activated in the grain where the m_{prism}/m_{basal} ratio is larger than 1.6.

3.5. TEM characterization

To validate the IGMA results, the nucleation and motion of $\langle a\rangle$-type dislocations in a prismatic plane were directly observed using *in-situ* TEM straining under a two-beam imaging condition. A grain, whose crystal orientation is identified to be (100.4, 104, −26.3), was selected for dislocation analysis. The Euler angles of grain and Burgers vector of dislocations were identified by analyzing two invisible diffraction conditions (Fig. 13a and b). The tensile axis is nearly parallel to the $\langle 10\bar{1}0\rangle$ axis, which is a representative case of tensile stretching of a basal-oriented grain in sheet alloy. With such a grain orientation, the m_{basal} is only 0.015 for basal dislocation slip $(01\bar{1}0)[\bar{2}110]$ but the m_{prism} is 0.41 for prismatic slip, resulting in high m_{prism}/m_{basal} of 27.3. According to the IGMA shown in Sections 3.2 and 3.3, the dominant dislocation mode of this grain should be the prismatic slip. Under $\boldsymbol{g} = 10\bar{1}1$ diffraction condition (Fig. 13c), the dislocations

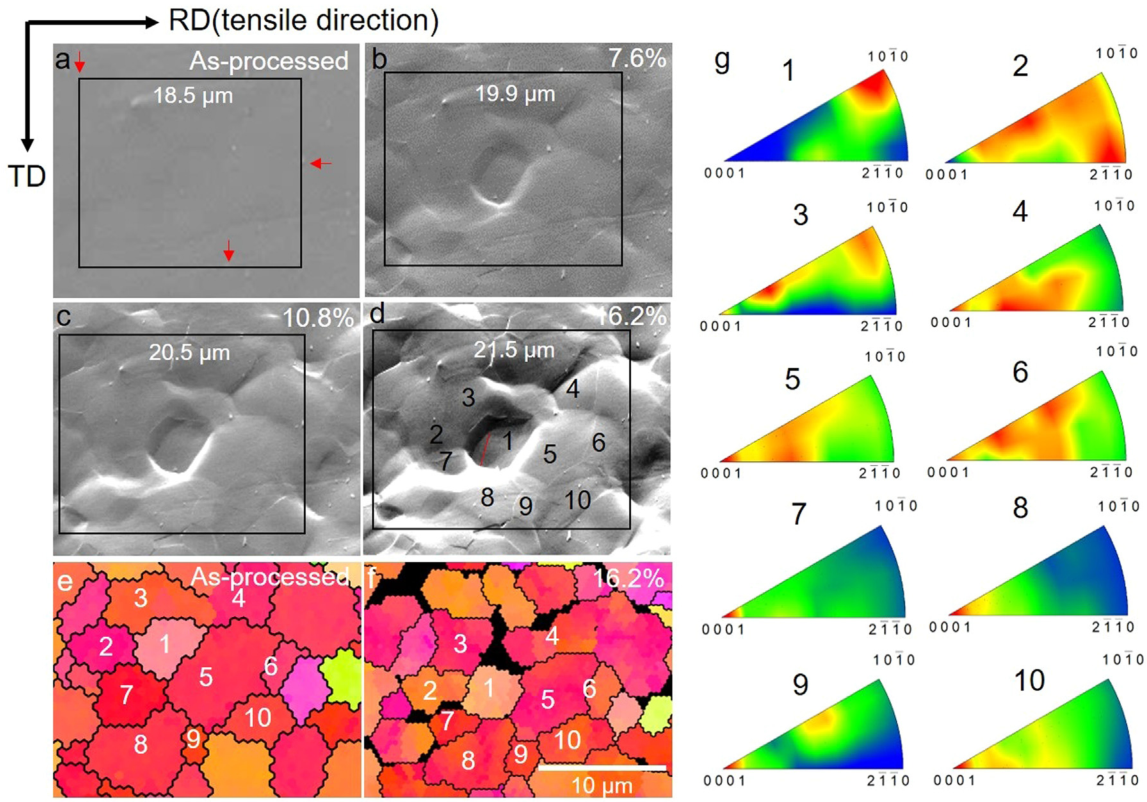

Fig. 12. *In-situ* observation of deformation and in-grain misorientation analysis of selected grains during tension. (a–d) SEM surface observation at the as-processed stage and subjected to 7.6%, 10.8% and 16.2% elongation. Red arrows in (a) highlight the surface features that have been used to track the same area in the black frames. The local strain is calculated based on the shape change of the black frames. (e, f) EBSD orientation maps at the as-processed stage and after 16.2% elongation. (g) Inverse pole figures showing IGMA distributions of each grain after 16.2% elongation.

Table 4
Schmid factor of the ten selected grains in Fig. 12.

Grain	φ (°)	Slip trace	Schmid factor		
			Basal	Prismatic	m_{prism}/m_{basal}
1	35	Basal	0.42	0.37	0.9
2	18.4	No trace	0.28	0.45	1.6
3	13.8	No trace	0.22	0.45	2.0
4	17.9	No trace	0.19	0.40	2.1
5	11.8	No trace	0.18	0.46	2.6
6	19.1	No trace	0.14	0.46	3.3
7	3.9	No trace	0.06	0.50	8.3
8	10.6	No trace	0.03	0.44	14.7
9	7.6	No trace	0.09	0.45	5.0
10	13.4	No trace	0.11	0.46	4.2

are visible. Several small loops on the prismatic plane were observed. The *in-situ* TEM characterization (Supplementary video 6) shows that they are transient sources, leading to intense dislocation multiplication and the formation of debris, most of the time small loops. Apart from ⟨a⟩-type dislocations, some dislocations in Fig. 13a and d are visible under $\boldsymbol{g} = 0002$ two-beam condition, indicating that they are either [c] or $\langle c + a\rangle$ dislocations. Essentially, dislocations that are visible under $\boldsymbol{g} = 0002$ condition are not frequently observed, and these [c] or $\langle c + a\rangle$ dislocations are not mobile during *in-situ* TEM characterization.

In contrast, glissile prismatic dislocation slip was frequently observed. Snapshots of *in-situ* TEM observation (Supplementary video 6) show that two dislocations in the grain in Fig. 14a–c have straight screw segments, indicating strong lattice friction. These two rectilinear ⟨a⟩ dislocations moved in the prismatic plane in opposite directions eventually leading to their annihilation at 0.92 s (Fig. 14b). Incomplete annihilation highlights however the presence of a sessile segment (in the red inset) that acts as a source from where the dislocation loop can spiral around. Such segments originate from the double cross-slip phenomenon, presumably from prismatic to the

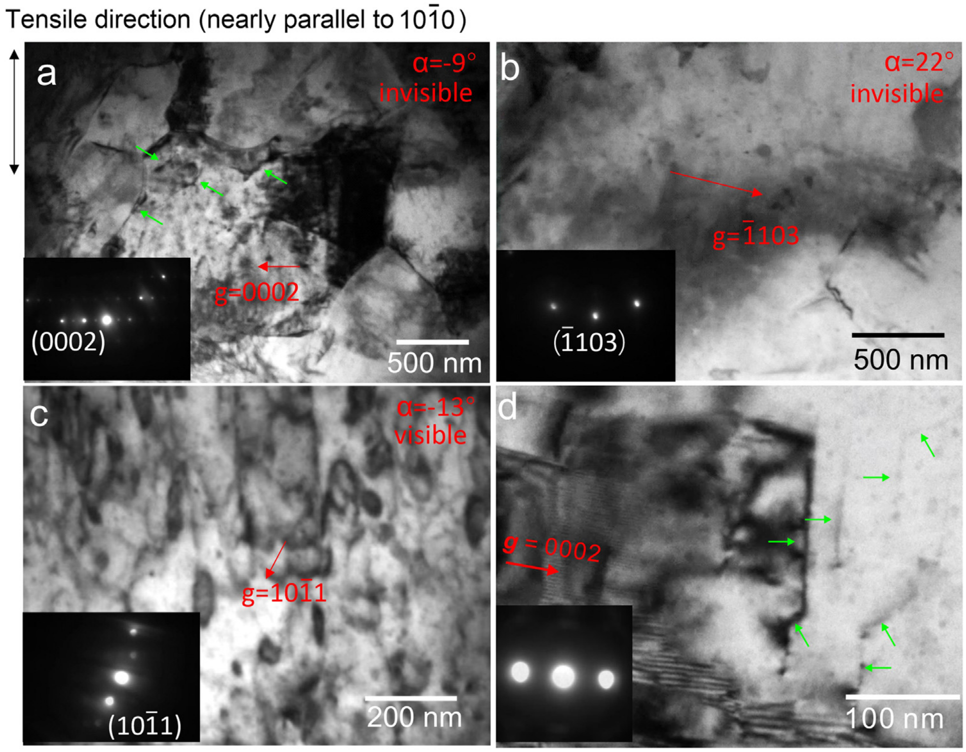

Fig. 13. TEM images of as-processed AZ31 sheet at different diffraction conditions, (a) $\boldsymbol{g_1} = 0002$, (b) $\boldsymbol{g_2} = \bar{1}013$, and (c) $\boldsymbol{g_3} = 10\bar{1}1$. The most dislocations in (c) were invisible with $\boldsymbol{g_1} = 0002$ and $\boldsymbol{g_2} = \bar{1}013$, and therefore, the Burgers vector of these dislocations is [11$\bar{2}$0]. (d) visible dislocation and stacking fault under $g = 0002$ condition at higher magnification. Green arrows in (a) and (d) show visible dislocations under $\boldsymbol{g_1} = 0002$ condition, indicating that they are either [c] or $\langle c + a \rangle$. The incident beam is nearly parallel to the [$\bar{1}2\bar{1}0$] of the matrix. The *in-situ* TEM images from Supplementary Video 6 were captured with diffraction condition of $\boldsymbol{g_3} = 10\bar{1}1$.

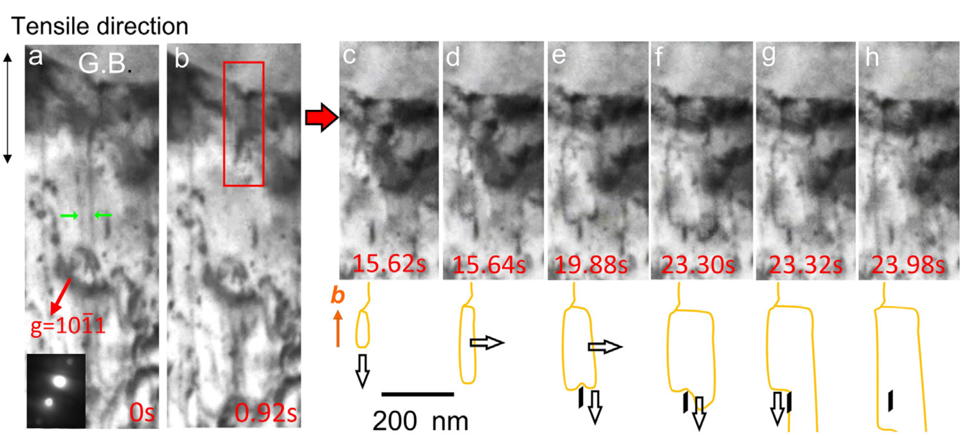

Fig. 14. *In-situ* TEM image sequences and corresponding schematic illustration of dislocation behavior. (a, b) annihilation of rectilinear screw components of $\langle a \rangle$ dislocations in the prismatic plane. In the inset (b) is shown a sessile segment that remains after annihilation and acts as a source of further dislocation (c–h). The incident beam is nearly parallel to [$\bar{1}2\bar{1}0$] of the matrix, and $\boldsymbol{g} = 10\bar{1}1$.

basal plane, due to solute atoms and precipitates, similar to what was observed in body-center cubic metals [75,76]. During multiplication, the strong screw/edge mobility anisotropy leads to the formation of a long screw dipole trailed by a curved faster edge segment, as demonstrated in Fig. 14c–h. Along its path (~150 nm between 15.62 s and 15.64 s) the edge dislocation is pinned by a nano-particle (Fig. 14e–g). After 23.98 s, the prismatic loop bypassed the nano-particle and the screw component became rectilinear again (Fig. 14h). The dislocation nucleation, motion, and annihilation shown in Fig. 12a–h repeatedly happen with deformation.

Given that the particles have an interaction with dislocations and thus affect the plastic deformation of the short-processed AZ31 sample, they are further characterized using STEM and EDX (Fig. 15). These particles have a spherical shape. Measured by ImageJ software, the size of particles is about 17.8 ± 6.3 nm in diameter. The EDX mappings show that these particles are predominantly Al-Mn particles.

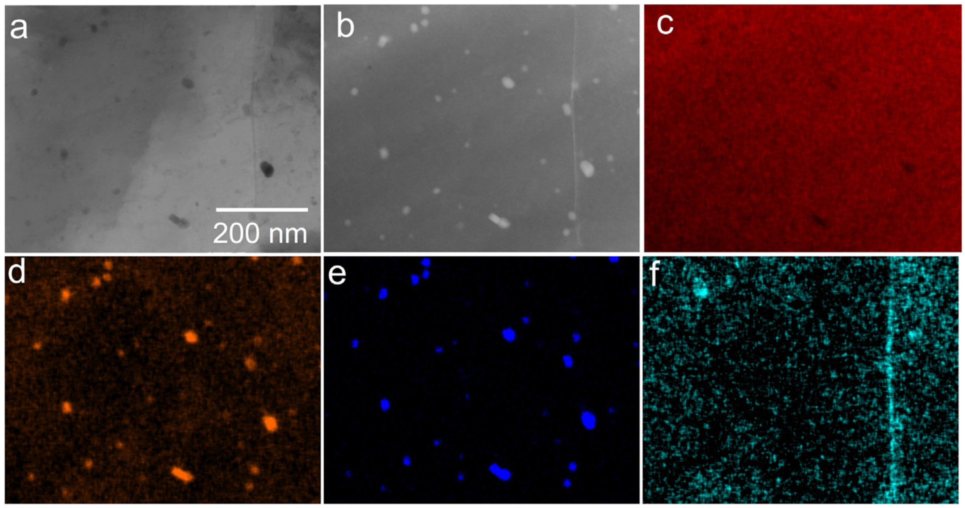

Fig. 15. (a) bright field and (b) high-angle annular dark field images, and EDX elemental mapping of (c) Mg, (d) Al, (e) Mn, (f) Zn element in the short-processed AZ31 sheet.

The existence of Al_8Mn_5 particles has been widely reported in Mg-Al-(Zn)-Mn alloys [77–79]. The volume fraction of Al-Mn nano-particles, obtained from thermodynamic (PANDAT® version 2020) calculation, is about 0.25%. This value is consistent with the previous publication [80].

4. Discussion

Based on the *in-situ* SEM, EBSD and TEM observation in bending and tensile testing, the origin of appreciable ductility and high bend formability in the strong-basal-texture AZ31 sheet can be discussed. In previous studies, the high ductility and formability of Mg alloys have been commonly interpreted as the result of texture weakening [9], heterogeneous grain size [48,81], GBS [30], twinning [82,83] and enhanced activity of pyramidal $\langle c + a\rangle$ dislocation [33]. Apparently, the bendable AZ31 sheet in this study has a strong basal texture and uniform grain size, but the grain size (~4.8 μm) is too large for GBS to be the dominant deformation mode in AZ31 at room temperature [51]. Due to the strong basal texture, extension twins form predominantly within the compression regions, and thus can hardly contribute to the plastic deformation of the tensile region. As demonstrated by the FEM simulation (Fig. 4), the total strain of the tensile region is even larger than the compression region. Therefore, the mechanism of the high bend formability should be more related to dislocation slip, rather than twinning. Regarding basal slip, it operates in the soft-oriented grains, as demonstrated by basal slip traces. However, these grains only take a minor fraction of all deformed grains. Numerous grains were deformed but without any visible slip traces. Regarding $\langle c + a\rangle$ dislocation, the observation of dislocations with a $\boldsymbol{c}$-component was marginal compared to ⟨a⟩ dislocations. As shown Fig. 13, these dislocations with $\boldsymbol{c}$-component do not move during *in-situ* TEM characterization. Furthermore, it has been reported that Al and Zn elements are detrimental to $\langle c + a\rangle$ cross-slip thus limiting their multiplication by the same mechanisms observed here for prismatic slip [33]. Therefore, $\langle c + a\rangle$ slip is unlikely to be the main reason for the enhanced ductility and bend formability of the AZ31 sheet.

4.1. CRSS ratio effect

Herein, an alternative explanation is proposed that for the strong-basal-texture Mg sheet alloys, the highly active and mobile ⟨a⟩-type dislocations, particularly those loops slipping on the prismatic crystal planes, are critical to the sheet ductility and bend formability. Although prismatic slip was previously reported to be a major deformation mode in the strong-basal-texture Mg [71,72], how the prismatic slip originates and how to manipulate the prismatic slip activity to achieve higher formability are still unclear. Based on the experimental observation, it is now clear that prismatic slip forms from the small dislocation loops on prismatic planes, and the low $CRSS_{prism}/CRSS_{basal}$ ratio is proposed to be an important reason for the active prismatic slip. Koike *et.al.* proposed that the higher prismatic slip activity in the fine-grained Mg alloy is caused by higher amount of grain boundaries which enhance compatibility stress at grain boundaries [84]. For quantitatively assessing the microstructural effect on prismatic slip, it was proposed that the effective CRSS of any dislocation slip system is not only depending on its intrinsic CRSS value, τ_c, which is normally measured from single crystal, but is also affected by internal reaction stress caused by dislocations, grain boundaries, and second-phase particles [85]. The dislocation can glide only when the effective CRSS is larger than the intrinsic CRSS plus the internal reaction stress. The magnitude of the internal reaction stress should be similar to different slip systems [85]. Effective CRSS ratio is

$$\frac{CRSS_{prism}}{CRSS_{basal}} = \frac{\tau_{c,prism} + \tau_{dis} + \tau_{particle} + \tau_{gb}}{\tau_{c,basal} + \tau_{dis} + \tau_{particle} + \tau_{gb}} \quad (3)$$

where τ_{dis}, $\tau_{particle}$, and τ_{gb} are the terms for the internal shear stress by dislocations, particles, and grain boundaries, respectively.

The internal reaction stress caused by grain boundary, τ_{gb}, could be expressed by a modified version of the Hall-Petch relationship in terms of grain size D (4.8 μm, measured by EBSD),

$$\tau_{\mathrm{gb}}=\frac{k}{\mathrm{M}\sqrt{D}} \tag{4}$$

where coefficient k equals 281 MPa/μm$^{1/2}$ for AZ31 rolling sheet [47] and M is the Taylor factor ($M = 2.5$) [86,87] for strong-basal-textured Mg. The grain boundary hardening, τ_{GB}, was calculated to be 51 MPa.

The internal shear stress caused by particles, $\tau_{particle,}$ can be expressed using the Orowan equation [88],

$$\tau_{\mathrm{particle}} = \frac{\mathrm{Gb}}{2\pi\sqrt{1-\nu}\left(\frac{0.779}{\sqrt{\mathrm{f}}}-0.785\right)\mathrm{D_P}}\ln\left(0.785\frac{\mathrm{D_P}}{\mathrm{b}}\right) \tag{5}$$

where ν is Poisson's ratio (≈0.289) [89], and b is the magnitude of Burgers vector of dislocation. Eq. (5) is based on the assumption that the uniformly-distributed Al-Mn nanoparticles have spherical shape [80], and the aspect ratio effect on dislocation slip, as reported in previous studies [13,88,90], is marginal. Given the dislocations in the short-processed AZ31 are found predominantly basal ⟨a⟩ and prismatic ⟨a⟩ type dislocations, Burgers vector with $b = 0.32$ nm for the basal slip can be used. G is the shear modulus (17 GPa). $\mathrm{D_P}$ is the mean planar diameter of the precipitate, ∼17.5 nm on average, which was directly measured from the STEM images (Fig. 15). The volume fraction of Al-Mn nano-particles, *f*, can be obtained from the thermodynamic calculation, about 0.25%. The resultant $\tau_{particle}$ is then calculated to be 14 MPa.

The internal reaction stress caused by dislocations, τ_{dis}, can be calculated using the Taylor relationship [91]

$$\mathrm{T}_{dis} = \alpha G b \rho^{1/2} \tag{6}$$

where ρ is dislocation density, measured by aforementioned e-CMWP method, about 5 × 10^{13} m^{-2}. Then, the τ_{dis} was calculated to be only 7.7 MPa, when coefficient α equals 0.2 [91]. It should be noted that the strain-hardening effects caused by the entanglement of basal-basal dislocations and basal-prismatic dislocations are different, even though both basal and prismatic dislocations have the same Burgers vector (***a***). However, the constant α is different for different types of dislocation interaction is different: for Mg deformed at room temperature, the measured α value is 0.2 for basal-basal dislocations interaction and 1.0 for basal-prismatic dislocation interaction [92]. Given that the basal and prismatic dislocations slips are the two predominant modes, two extreme scenarios are hypothesized: when the dislocation interaction is fully basal-basal interaction, then the τdis was calculated to be only 7.7 MPa. When the dislocation interaction is fully basal-prismatic interaction, then the τ_{dis} was calculated to be only 38.5 MPa. Therefore, the τ_{dis} should be in the range between 7.7 MPa and 38.5 MPa.

Having calculated the values of τ_{dis}, $\tau_{particle}$, and τ_{gb} based on Eqs. (3)–(6), the effective $CRSS_{prism}/CRSS_{basal}$ ratio of the short-processed AZ31 sheet was calculated to be between 1.4 and 1.6, depending on the fraction of basal-basal and basal-prismatic dislocation interaction. This is very close to the IGMA result (1.5∼1.6) based on the *in-situ* EBSD characterization. However, at the current stage, it is very challenging to quantitatively identify the fraction of basal-basal and basal-prismatic dislocation interaction, but the calculation shows a similar values of $CRSS_{prism}/CRSS_{basal}$ ratio, regardless of how dislocations interact with each other. This situation happens when other factors, such as grain boundaries, are the major contributor to the hardening effect.

In addition to the good agreement in this study, Fig. 16a shows that the calculated $CRSS_{prism}/CRSS_{basal}$ values are also close to those reported in the literature [93,94] when the dislocation density of the annealed Mg and AZ31 alloy is estimated to be about 1 × 10^{13} m^{-2} [95,96]. The low $CRSS_{prism}/CRSS_{basal}$ value of short-processed AZ31 sheet measured and calculated in this study can also be supported by the high anisotropy *r*-value measured from *in-situ* (∼2.2) and *ex-situ* (∼2.0) testing, as significant prismatic slip is responsible for the high anisotropy of strong-basal-textured Mg alloy [26,71,72]. Polycrystal plasticity simulations of AZ31 sheet indicate a strong relationship between $CRSS_{prism}/CRSS_{basal}$ and the predicted *r*-values, and show that $CRSS_{prism}/CRSS_{basal}$ value is about 1.5 when the *r*-value is ∼2 in the tensile testing along the RD [72].

Fig. 16b further illustrates that the activity of prismatic slip can be effectively enhanced by grain boundary hardening when the residual strain is low and the particle hardening effect is marginal. With larger grain sizes, the $CRSS_{prism}/CRSS_{basal}$ ratio becomes much higher when the dislocation density is low. This can well explain the lower formability in bending of fully anneal Mg alloy sheet reported in the literature [3], which normally has a much larger grain size, e.g. 50 μm in diameter [97]. Therefore, grain refinement is desired to reduce the $CRSS_{prism}/CRSS_{basal}$ ratio and enhance the sheet ductility and bend formability.

4.2. Residual strain effect

By examining the elongation data about a large amount of rolled and extruded Mg alloys (data compiled from Ref. [9], a general trend of decreasing elongation with the larger grain size can be observed, when the grain sizes of alloy are larger than ∼30 μm (Fig. 17a). This phenomenon can be justified with the finding of this study that larger grain leads to higher $CRSS_{prism}/CRSS_{basal}$ ratio and thus lower activity of prismatic slip. However, Fig. 17a also shows that smaller grains do not necessarily lead to higher elongation. Instead, the high elongation occurs frequently with the grain size between 10 and 20 μm. For the extruded and rolled AZ31 alloy (Fig. 17b), the highest elongation occurs when the grain size is ∼15 μm. When the AZ31 alloys reported in the literature have grain sizes of ∼5 μm, the ductility is much lower.

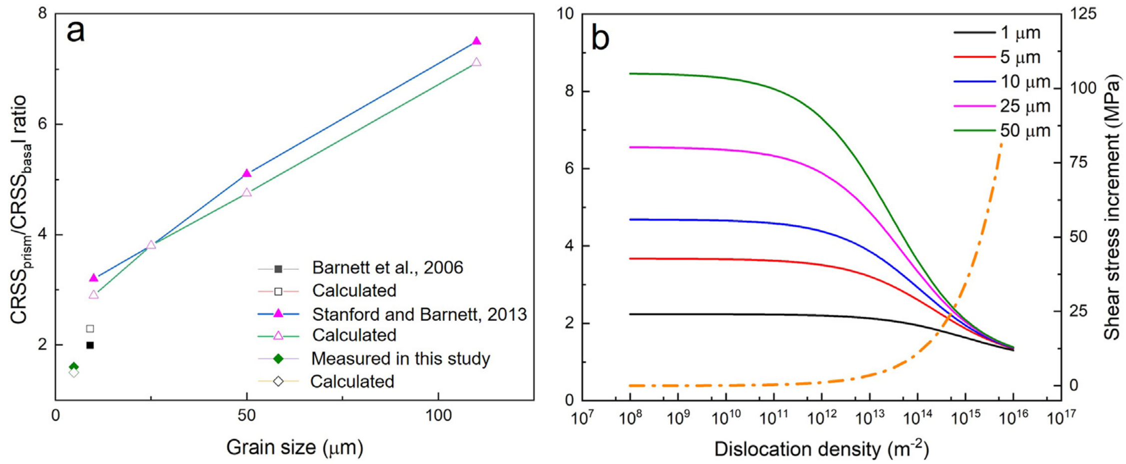

Fig. 16. (a) Data shows a good match about the $CRSS_{prism}/CRSS_{basal}$ ratio in this study and literature [93,94]. (b) $CRSS_{prism}/CRSS_{basal}$ ratio as functions of grain size and dislocation density, and the increment in shear stress by dislocations as a function of dislocation density.

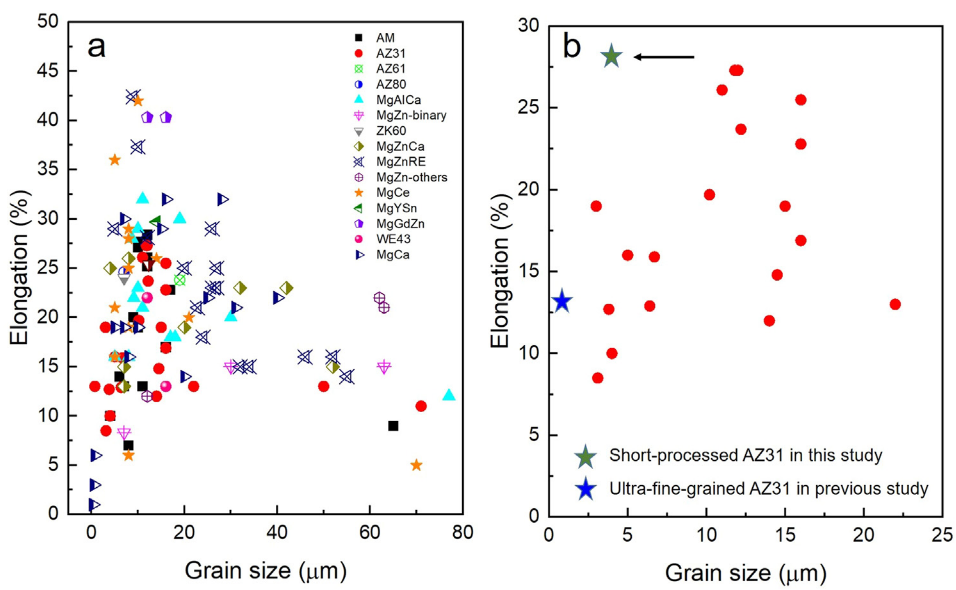

Fig. 17. Data from the literature review [9] about elongations and grain sizes of (a) Mg extruded and rolled alloys and (b) specifically AZ31 alloy extruded and rolled under different conditions.

In order to clarify the factor that causes lower ductility with the small grain size reported in the literature, the ultra-fine-grained AZ31 developed in our previous study [51] is revisited and used as a representative to compare with the short-processed AZ31 in this study. This low-temperature-extruded AZ31 also have equiaxed grains with an average grain size of 0.65 μm in diameter [51]. However, its microstrain and residual dislocation density are much higher than those of the short-processed AZ31 in this study, revealed by XRD characterization. Using Eq. (2), the microstrain of the low-temperature extruded AZ31 is 0.0153 (Fig. 18a), about 3 times more than that of the short-processed AZ31 in this study (0.004). By fitting the XRD spectrum of low-temperature extruded AZ31 sample using the aforementioned e-CMWP method, the dislocation density is estimated to be ~5.3 × 10^{14} m^{-2} (Fig. 18b), 10 times higher than that of the short-processed AZ31 in this study (~5 × 10^{13} m^{-2}. With such a higher dislocation density, the hardening caused by residual strain τ_{dis} is increased to 27~135 MPa in the low-temperature extruded AZ31 sample, and its strain hardening capacity during subsequent tensile testing is greatly reduced (demonstrated by low strain hardening exponent of 0.05 [51] whilst the low strain hardening exponent of short-processed AZ31 is 0.16). The high residual strain should limit the ductility of the ultra-fine-grained AZ31 extrusion.

Regarding $CRSS_{prism}/CRSS_{basal}$ ratio effect, the $CRSS_{prism}/CRSS_{basal}$ ratio of the ultra-fine-grained AZ31 extrusion (1.20~1.30) is just slightly lower than that of the short-processed AZ31 alloy (1.40~1.58). Therefore, the $CRSS_{prism}/CRSS_{basal}$ ratio should not be the reason, when the significant difference in ductility between the low-temperature-extruded and short-processed AZ31 alloys is discussed. This also suggests if high density of dislocations and precipitates have already induced significant hardening,

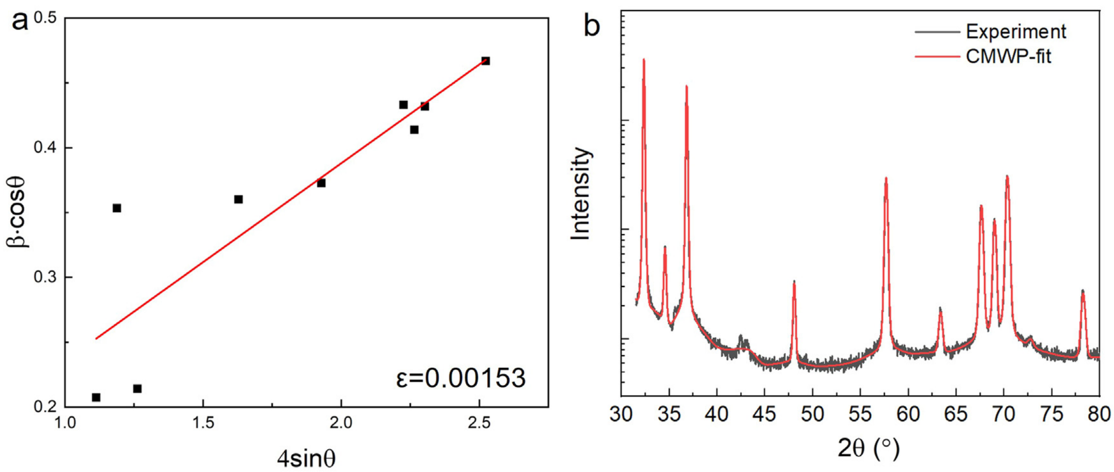

Fig. 18. (a) Calculation of micro-strain based on the peak broadening using the Williamson–Hall method and (b) experimental measured and CMWP-fit XRD spectra of low-temperature-extruded AZ31 in our previous study [51].

the grain size effect on the relative activity of slip modes is expected to be insignificant.

In metal engineering, simultaneously achieving refined grain size and low residual strain in a uniform manner is technically challenging. The refinement of grain size by severe plastic deformation [98] or low-temperature extrusion [51] inevitably induces high residual strain, but post-deformation annealing often leads to significant grain growth. This study provides a feasible approach to overcoming the tradeoff between residual strain and grain size. In Mg alloy, grain refinement does not necessarily decrease ductility. Instead, higher plasticity could be achieved with finer grain size [43], due to relatively easier activation of prismatic slip to basal slip and more uniform strain distribution during plastic deformation [99]. In this study, the Al-Mn nanoparticles should also play an important role. Although the particle effect on decreasing the effective $CRSS_{prism}/CRSS_{basal}$ ratio is much less significant than the grain boundary effect, the pre-existing ⟨a⟩ screw dislocations were likely to bypass the nano-particles during motion, leaving debris that leads to easy multiplication. The mechanism of dislocation multiplication from loops on the prismatic plane has been reported by Couret et al. [100]. Apparently, the Al-Mn nanoparticles provide numerous sites for generating dislocation loops, which in turn are the sources of mobile prismatic dislocation slip. The enhanced activity of prismatic ⟨a⟩ dislocations can thus effectively accommodate plastic deformation in basal-oriented grains, should enhance ductility and bend formability.

The effective operation of prismatic slip provides a minimum of four independent slip systems, and can accommodate appreciable plastic strain when deformation along the RD is the major mode, as demonstrated in this study. It should be noted, however, when the deformation along the ND is dominant, a fifth independent slip mode (e.g. $\langle c + a \rangle$ slip) is required to allow crystals to compress along their **c**-axis to achieve appreciable formability in the strong-basal-textured Mg alloy sheet [72]. Alternatively, the basal texture should be weakened, allowing the active basal slip to accommodate strain along the ND. In previous studies [23,101], the high stretch formability in cupping test was achieved in a Mg-Al-Sn [23] and Mg-Al-Zn-Ca [101] alloy sheets, reportedly due to high prismatic slip activity. However, these Sn- and Ca-containing alloy sheets had much weaker basal texture than AZ31 alloy sheet. Therefore, whether the texture weakening or enhanced prismatic slip activity is the key factor for the improved stretch formability needs to be further clarified. Nevertheless, for the applications that high ductility and bend formability, rather than press formability, are required (e.g. hemming process in the automotive manufacturing), it is not mandatory to weaken basal texture [28], refine grain size to submicron scale under extreme processing conditions [30], or decrease alloying concentration to very dilute levels [31]. Instead, the key to achieving high bend formability of the sheet is to simultaneously minimize residual strain and keep the refined grain size uniformly around several microns via optimizing the combination of strain, strain rate, and temperature in the manufacturing process. It is proposed that different to conventional rolling, which starts from as-cast ingot and with cold rolling wheels, the simultaneously achieving low residual strain and refined grains of the as-rolled sheet in this study is caused by the combined effects of refined microstructure of feedstock, i.e. the plate which has already extruded at high temperature and by large strain, as well as warm temperature during deformation (around 210∼260 °C), by i.e. in-line heating of rolling wheels and supports. The in-line heating has promoted the dynamic recovery and recrystallisation, but avoid grain growth. The this manuscript has demonstrated that it is possible to simultaneously achieve low residual strain and refined grains, but the optimized processing parameter is still to be determined in future studies.

5. Conclusions

In this study, a short manufacturing process, which is composed of a large-strain extrusion and subsequent warm rolling,

Please cite this article as: S. Xu, P. Xiao, X. Wu et al., Mechanistic investigation of highly bendable magnesium alloy sheet fabricated by short-process manufacturing, Journal of Magnesium and Alloys, https://doi.org/10.1016/j.jma.2023.09.026

is developed to produce ductile and bendable AZ31 thin sheet. The bending deformation is simulated using FEM. Its deformation mode during tensile and bend tests is investigated by monitoring its microstructural evolution using multi-scale *in-situ* SEM, EBSD, and TEM. The main conclusions are listed as follows.

(1) The short-processed AZ31 sheet is ductile and exhibits outstanding formability in bending tests even without annealing. The strength and total elongations are 224 MPa and 27%, respectively, higher than those of its as-extruded counterpart. Its minimum bend radius is as small as 0.2T in the 90° cold bending test, much smaller than that of the as-extruded strip (∼3.3T).
(2) The short-processed AZ31 sheet withstands bending-flattening and then reverse bending with a small bending radius (4T). In the compression region of the sample, extension twin bands formed during bending, but they disappeared via detwinning upon flattening. The detwinning alleviated the local high strain associated with the twin bands and led to slowly increased and uniformly distributed strain, allowing the possibility of further bending.
(3) The short manufacturing process can simultaneously achieve refined grain size and low residual strain uniformly, by comparing with the AZ31 extruded and rolled under different conditions. Such a microstructure leads to an appreciable work hardening capacity and uniform plastic deformation in the subsequent tension and bending, and therefore postpones the occurrence of in-grain cracking and strain localization along the TD.
(4) For the AZ31 sheet with a strong basal texture, the appreciable ductility and outstanding bend formability originate from the significant ⟨a⟩-type dislocation loops slipping on the prismatic crystal planes within dynamic-recrystallized grains that are refined to several microns. The active prismatic dislocation slip was caused by its much lower relative activation stress to basal slip ($CRSS_{prism}$/ $CRSS_{basal}$ of only ∼1.6) owing to the effective grain boundary hardening. The prismatic dislocation activity is further enhanced when they bypass Al-Mn nano-particles during motion, leaving debris that leads to easy multiplication.

Author contributions

S.W.X. performed *in-situ* SEM and EBSD characterization and wrote the manuscript. X.F.W. performed the FEM simulation. J.H. contributed to the digital image correlation. F.M. performed *in-situ* TEM characterization. Z.Y.X. performed the XRD characterization. Z.H.L. and C.J. performed the casting, extrusion, and rolling of the AZ31 sheet. T.J.L. contributed to the programming of slip trace analysis. K.S.W. participated in the project and provided proofreading of the manuscript. Z.R.Z. interpreted the results, coordinated the project, and revised the manuscript.

Data availability

The authors declare that the main data supporting the findings of this study are available within the article and its Supplementary Information files. Extra data are available from the corresponding author upon request.

Declaration of Competing Interest

The authors declare that they have no known competing financial interests or personal relationships that could have appeared to influence the work reported in this paper.

Acknowledgements

The authors are thankful for the helpful discussion with Dr Huizhi Peng, Dr Yuman Zhu and Prof. Nick Birbilis. This work is the financial supported by the Science and Technology Innovation Program of Hunan Province (2020RC4013 and 2021JC0005), “Technology Innovation 2025” Major Special Project of Ningbo City, the Joint Funds of the National Natural Science Foundation of China (U22A20187), the Future Fellowship of the Australian National University.

Supplementary materials

Supplementary material associated with this article can be found, in the online version, at doi:10.1016/j.jma.2023.09.026.

References

[1] I. Polmear, D. StJohn, J.F. Nie, M. Qian, Light Alloys, 5th ed., Butterworth-Heinemann, Boston, 2017.
[2] S. Kobayashi, S. Plotkin, S.K. Ribeiro, Energ. Effic. 2 (2) (2009) 125–137.
[3] M.M. Avedesian, H. Baker, ASM Specialty Handbook - Magnesium and Magnesium Alloys, ASM International, Materials Park, OH, 1999.
[4] H.E. Friedrich, B.L. Mordike, in: Technology of Magnesium and Magnesium Alloys, Magnesium Technology: Metallurgy, Design Data, Applications, Springer Berlin Heidelberg, Berlin, Heidelberg, 2006, pp. 219–430.
[5] O.M. Ikumapayi, E.T. Akinlabi, N. Madushele, S.O. Fatoba, in: A Brief Overview of Bending Operation in Sheet Metal Forming, Springer Singapore, Singapore, 2020, pp. 149–159.
[6] M.P. Groover, Fundamentals of Modern Manufacturing: Materials, Processes, and Systems, John Wiley & Sons, 2020.
[7] S. Kalpakjian, S.R. Schmid, Manufacturing Engineering and Technology, 7th ed., Pearson, Singapore, 2014.
[8] J.R. Davis, ASM Specialty Handbook - Aluminum and Aluminum Alloys, ASM International, Materials Park, OH, 1993.
[9] J.F. Nie, K.S. Shin, Z.R. Zeng, Metall. Mater. Trans. A 51 (12) (2020) 6045–6109.
[10] J. Hirsch, T. Al-Samman, Acta Mater. 61 (3) (2013) 818–843.
[11] W. Wu, P. Zhang, X. Zeng, L. Jin, S. Yao, A.A. Luo, Mater. Sci. Eng. A 486 (1) (2008) 596–601.
[12] C. He, B. Jiang, Q. Wang, Y. Chai, J. Zhao, M. Yuan, G. Huang, D. Zhang, F. Pan, Mater. Sci. Eng. A 799 (2021) 140290.
[13] F. Wang, J.J. Bhattacharyya, S.R. Agnew, Mater. Sci. Eng. A 666 (2016) 114–122.

[14] M. Habibnejad-Korayem, M.K. Jain, R.K. Mishra, Mater. Sci. Eng. A 648 (2015) 371–384.
[15] S.H.M. Azghandi, M. Weiss, M.R. Barnett, JOM 72 (7) (2020) 2586–2596.
[16] C. He, L. Liu, S. Bai, B. Jiang, H. Teng, G. Huang, D. Zhang, F. Pan, Materials 15 (24) (2022) 8880.
[17] Y. Chino, M. Kado, M. Mabuchi, Mater. Sci. Eng. A 494 (1) (2008) 343–349.
[18] M.Z. Bian, T.T. Sasaki, B.C. Suh, T. Nakata, S. Kamado, K. Hono, Scr. Mater. 138 (2017) 151–155.
[19] T. Nakata, C. Xu, Y. Uehara, T.T. Sasaki, S. Kamado, J. Alloys Compd. 782 (2019) 304–314.
[20] T.T.T. Trang, J.H. Zhang, J.H. Kim, A. Zargaran, J.H. Hwang, B.C. Suh, N.J. Kim, Nat. Commun. 9 (1) (2018) 2522.
[21] J. Bohlen, M.R. Nürnberg, J.W. Senn, D. Letzig, S.R. Agnew, Acta Mater. 55 (6) (2007) 2101–2112.
[22] Z. Zeng, M. Zhou, P. Lynch, F. Mompiou, Q. Gu, M. Esmaily, Y. Yan, Y. Qiu, S. Xu, H. Fujii, C. Davies, J.F. Nie, N. Birbilis, Acta Mater. 206 (2021) 116648.
[23] B.C. Suh, J.H. Kim, J.H. Bae, J.H. Hwang, M.S. Shim, N.J. Kim, Acta Mater. 124 (2017) 268–279.
[24] J.Y. Lee, Y.S. Yun, B.C. Suh, N.J. Kim, W.T. Kim, D.H. Kim, J. Alloys Compd. 589 (2014) 240–246.
[25] T. Al-Samman, X. Li, Mater. Sci. Eng. A 528 (10) (2011) 3809–3822.
[26] S. Yi, J. Bohlen, F. Heinemann, D. Letzig, Acta Mater. 58 (2) (2010) 592–605.
[27] A. Nagendra, D. Steglich, Procedia Manuf. 47 (2020) 1274–1280.
[28] H. Koh, T. Sakai, H. Utsunomiya, S. Minamiguchi, Mater. Trans. 48 (8) (2007) 2023–2027.
[29] L.J. Cartmell, F. King, G. Salt, Met. Technol. 2 (1) (1975) 313–317.
[30] Z. Zeng, J.F. Nie, S.W. Xu, C.H.J. Davies, N. Birbilis, Nat. Commun. 8 (1) (2017) 972.
[31] H. Somekawa, A. Singh, Scr. Mater. 150 (2018) 26–30.
[32] R. Zheng, J.P. Du, S. Gao, H. Somekawa, S. Ogata, N. Tsuji, Acta Mater. 198 (2020) 35–46.
[33] Z. Wu, R. Ahmad, B. Yin, S. Sandlöbes, W.A. Curtin, Science 359 (6374) (2018) 447–452.
[34] S. Sandlöbes, S. Zaefferer, I. Schestakow, S. Yi, R. Gonzalez-Martinez, Acta Mater. 59 (2) (2011) 429–439.
[35] H. Ovri, J. Markmann, J. Barthel, M. Kruth, H. Dieringa, E.T. Lilleodden, Acta Mater. 244 (2023) 118550.
[36] Z.R. Zeng, M.Z. Bian, S.W. Xu, C.H.J. Davies, N. Birbilis, J.F. Nie, Mater. Sci. Eng. A 674 (2016) 459–471.
[37] D. Griffiths, Mater. Sci. Technol. 31 (1) (2015) 10–24.
[38] D. Guan, W.M. Rainforth, J. Gao, J. Sharp, B. Wynne, L. Ma, Acta Mater. 135 (2017) 14–24.
[39] I. Basu, T. Al-Samman, Acta Mater. 67 (2014) 116–133.
[40] X. Huang, K. Suzuki, A. Watazu, I. Shigematsu, N. Saito, J. Alloys Compd. 470 (1) (2009) 263–268.
[41] H. Watanabe, T. Mukai, K. Ishikawa, J. Mater. Proc. Technol. 182 (1) (2007) 644–647.
[42] W.J. Kim, J.D. Park, W.Y. Kim, J. Alloys Compd. 460 (1) (2008) 289–293.
[43] X. Luo, Z. Feng, T. Yu, J. Luo, T. Huang, G. Wu, N. Hansen, X. Huang, Acta Mater. 183 (2020) 398–407.
[44] J. Sun, L. Jin, J. Dong, F. Wang, S. Dong, W. Ding, A.A. Luo, Int. J. Plast. 123 (2019) 121–132.
[45] D.F. Shi, M.T. Pérez-Prado, C.M. Cepeda-Jiménez, Acta Mater. 180 (2019) 218–230.
[46] S.M. Razavi, D.C. Foley, I. Karaman, K.T. Hartwig, O. Duygulu, L.J. Kecskes, S.N. Mathaudhu, V.H. Hammond, Scr. Mater. 67 (5) (2012) 439–442.
[47] A. Jain, O. Duygulu, D.W. Brown, C.N. Tomé, S.R. Agnew, Mater. Sci. Eng. A 486 (1) (2008) 545–555.
[48] Z. Zhang, J. Zhang, W. Wang, S. Liu, B. Sun, J. Xie, T. xiao, Scr. Mater. 221 (2022) 114963.
[49] T. Wang, M. Zha, C. Du, H.L. Jia, C. Wang, K. Guan, Y. Gao, H.Y. Wang, Mater. Res. Lett. 11 (3) (2023) 187–195.
[50] W. Chen, W. He, B. Jiang, F. Pan, Int. J. Plast. 159 (2022) 103483.
[51] Z.R. Zeng, Y.M. Zhu, R.L. Liu, S.W. Xu, C.H.J. Davies, J.F. Nie, N. Birbilis, Acta Mater. 160 (2018) 97–108.
[52] J. Holmes, S. Sommacal, Z. Stachurski, R. Das, P. Compston, Compos. Struct. 279 (2022) 114775.
[53] F. Mompiou, R.X. Xie, J. Microsc. 282 (1) (2021) 84–97.
[54] C.D. Barrett, A. Imandoust, A.L. Oppedal, K. Inal, M.A. Tschopp, H. El Kadiri, Acta Mater. 128 (2017) 270–283.
[55] V.M. Miller, T.M. Pollock, Metall. Mater. Trans. A 47 (4) (2016) 1854–1864.
[56] G.K. Williamson, W.H. Hall, Acta Metall. 1 (1) (1953) 22–31.
[57] G. Ribárik, T. Ungár, J. Gubicza, J. Appl. Crystallogr. 34 (5) (2001) 669–676.
[58] G. Ribárik, B. Jóni, T. Ungár, Crystals 10 (7) (2020) 623.
[59] G. Ribárik, J. Gubicza, T. Ungár, Mater. Sci. Eng. A 387-389 (2004) 343–347.
[60] C. Lee, F. Maresca, R. Feng, Y. Chou, T. Ungar, M. Widom, K. An, J.D. Poplawsky, Y.C. Chou, P.K. Liaw, W.A. Curtin, Nat. Commun. 12 (1) (2021) 5474.
[61] Y. Zhu, K. Zhang, Z. Meng, K. Zhang, P. Hodgson, N. Birbilis, M. Weyland, H.L. Fraser, S.C.V. Lim, H. Peng, R. Yang, H. Wang, A. Huang, Nat. Mater. 21 (11) (2022) 1258–1262.
[62] M. Wang, X.Y. Xu, H.Y. Wang, L.H. He, M.X. Huang, Acta Mater. 201 (2020) 102–113.
[63] G. Ribárik, J. Gubicza, T. Ungár, 2023 http://csendes.elte.hu/cmwp/).
[64] I.C. Dragomir, T. Ungár, J. Appl. Crystallogr. 35 (5) (2002) 556–564.
[65] Z. Zeng, N. Stanford, C.H.J. Davies, J.F. Nie, N. Birbilis, Int. Mater. Rev. 64 (1) (2019) 27–62.
[66] T. Al-Samman, G. Gottstein, Mater. Sci. Eng. A 488 (1) (2008) 406–414.
[67] M.R. Barnett, Mater. Sci. Eng. A 464 (1) (2007) 8–16.
[68] P. Chen, F. Wang, B. Li, Acta Mater. 164 (2019) 440–453.
[69] Y.B. Chun, C.H.J. Davies, Metall. Mater. Trans. A 42 (13) (2011) 4113–4125.
[70] D. Xia, X. Chen, G. Huang, B. Jiang, A. Tang, H. Yang, S. Gavras, Y. Huang, N. Hort, F. Pan, Scr. Mater. 171 (2019) 31–35.
[71] J. Koike, R. Ohyama, Acta Mater. 53 (7) (2005) 1963–1972.
[72] S.R. Agnew, Ö. Duygulu, Int. J. Plast. 21 (6) (2005) 1161–1193.
[73] C.M. Cepeda-Jiménez, J.M. Molina-Aldareguia, M.T. Pérez-Prado, JOM 68 (1) (2016) 116–126.
[74] C.J. Boehlert, Z. Chen, I. Gutiérrez-Urrutia, J. Llorca, M.T. Pérez-Prado, Acta Mater. 60 (4) (2012) 1889–1904.
[75] F. Mompiou, D. Tingaud, Y. Chang, B. Gault, G. Dirras, Acta Mater. 161 (2018) 420–430.
[76] D. Caillard, Acta Mater. 61 (8) (2013) 2808–2827.
[77] S. Pawar, X. Zhou, T. Hashimoto, G.E. Thompson, G. Scamans, Z. Fan, J. Alloys Compd. 628 (2015) 195–198.
[78] P. Cao, D.H. StJohn, M. Qian, Mater. Sci. Forum 488-489 (2005) 139–142.
[79] G. Zeng, J.W. Xian, C.M. Gourlay, Acta Mater. 153 (2018) 364–376.
[80] N. Stanford, D. Atwell, Metall. Mater. Trans. A 44 (10) (2013) 4830–4843.
[81] M. Zha, X.H. Zhang, H. Zhang, J. Yao, C. Wang, H.Y. Wang, T.T. Feng, Q.C. Jiang, J. Alloys Compd. 765 (2018) 1228–1236.
[82] H. Fan, S. Aubry, A. Arsenlis, J.A. El-Awady, Scr. Mater. 112 (2016) 50–53.
[83] L. Jin, J. Dong, J. Sun, A.A. Luo, Int. J. Plast. 72 (2015) 218–232.
[84] J. Koike, T. Kobayashi, T. Mukai, H. Watanabe, M. Suzuki, K. Maruyama, K. Higashi, Acta Mater. 51 (7) (2003) 2055–2065.
[85] W.B. Hutchinson, M.R. Barnett, Scr. Mater. 63 (7) (2010) 737–740.
[86] C.H. Cáceres, P. Lukáč, Philos. Mag. 88 (7) (2008) 977–989.
[87] B. Guan, Y. Xin, X. Huang, P. Wu, Q. Liu, Acta Mater. 173 (2019) 142–152.
[88] J.F. Nie, Scr. Mater. 48 (8) (2003) 1009–1015.
[89] Y. Wang, H. Choo, Acta Mater. 81 (2014) 83–97.
[90] J.D. Robson, N. Stanford, M.R. Barnett, Acta Mater. 59 (5) (2011) 1945–1956.

Please cite this article as: S. Xu, P. Xiao, X. Wu et al., Mechanistic investigation of highly bendable magnesium alloy sheet fabricated by short-process manufacturing, Journal of Magnesium and Alloys, https://doi.org/10.1016/j.jma.2023.09.026

[91] D. Hull, D. Bacon, Introduction to Dislocations, 4th ed., Butterworth-Heinemann, Oxford, 2001.
[92] F.F. Lavrentev, Mater. Sci. Eng. 46 (2) (1980) 191–208.
[93] M.R. Barnett, Z. Keshavarz, X. Ma, Metall. Mater. Trans. A 37 (7) (2006) 2283–2293.
[94] N. Stanford, M.R. Barnett, Int. J. Plast. 47 (2013) 165–181.
[95] K. Wei, R. Hu, D. Yin, L. Xiao, S. Pang, Y. Cao, H. Zhou, Y. Zhao, Y. Zhu, Acta Mater. 206 (2021) 116604.
[96] M.P. Miles, D. Fullwood, B.L. Adams, A. Khosravani, J. Scott, R.K. Mishra, J. Mater. Eng. Perform. 20 (8) (2011) 1357–1363.
[97] S.R. Agnew, C.N. Tomé, D.W. Brown, T.M. Holden, S.C. Vogel, Scr. Mater. 48 (8) (2003) 1003–1008.
[98] R. Valiev, Nat. Mater. 3 (8) (2004) 511–516.
[99] Z. Zhang, J.H. Zhang, J. Wang, Z.H. Li, J.S. Xie, S.J. Liu, K. Guan, R.Z. Wu, Int. J. Miner. Metall. Mater. 28 (1) (2021) 30–45.
[100] A. Couret, D. Caillard, Acta Metall. 33 (8) (1985) 1447–1454.
[101] U.M. Chaudry, Y.S. Kim, K. Hamad, Mater. Lett. 238 (2019) 305–308.

Please cite this article as: S. Xu, P. Xiao, X. Wu et al., Mechanistic investigation of highly bendable magnesium alloy sheet fabricated by short-process manufacturing, Journal of Magnesium and Alloys, https://doi.org/10.1016/j.jma.2023.09.026